

ALGORITHMS TO ASSESS STRUCTURAL AND FUNCTIONAL REMODELING  
SURROUNDING NEURAL PROSTHESIS

By

Akash Saxena

A THESIS

Submitted to  
Michigan State University  
in partial fulfillment of the requirements  
for the degree of

Electrical Engineering - Master of Science

2020

## ABSTRACT

### ALGORITHMS TO ASSESS STRUCTURAL AND FUNCTIONAL REMODELING SURROUNDING NEURAL PROSTHESIS

By

Akash Saxena

Recorded signals from implanted electrodes in the brain can be used to restore motor function for patients suffering from neurological injuries or neurodegenerative diseases, either through decoding the signal to control exterior assistive devices or as a trigger for downstream neurostimulation. However, an ongoing challenge in the field is the limited and unpredictable ability to record from neural prosthesis for longer periods of time due to the biological response from the brain, the technical issues related to the signal processing algorithms used, and the stability of the microelectrode itself. Our lab has recently uncovered multiple new observations of structural and functional remodeling of neurons surrounding implanted electrodes, which may contribute to the instability in recording quality over time. Some of these observations indicate losses, or changes, in synaptic connectivity of individual local neurons with the surrounding network. In this thesis, I have introduced signal processing tools which will help us to understand and characterize the structural and functional remodeling happening around the neural prosthesis, through the incorporation of multi-unit activity, coherence analysis, spike-triggered average of the local field potential, and spike triggered covariance of the local field potential. A better understanding of these changes can provide us with new insights into how the network is remodeling itself over time and the major factors which influence these processes, which will help us to enable the design of better and more biocompatible neural prostheses.

## ACKNOWLEDGEMENTS

I would like to thank Dr. Erin Purcell, for always encouraging me, providing her excellent guidance towards bridging the gap between electrical engineering and neuroscience and making it a fun experience, this research would not have been possible without her. I would also like to thank the members of the lab for always supporting me and taking care of me both inside and outside the lab.

## TABLE OF CONTENTS

LIST OF TABLES	iv
LIST OF FIGURES	v
CHAPTER 1 INTRODUCTION	1
1. Overview of neuronal structure and function	1
1.1. Signal generation of a neuron	1
1.2. Transmission of neuronal signals	4
2. Extracellular signal detection by implanted electrodes	6
2.1. Neuronal geometry and architecture	8
2.2. Temporal scaling properties	10
2.3. Role of volume conduction	10
3. Implanted electrodes in brain: Progress and challenges	11
3.1. Silicon based microelectrodes	12
3.2. Challenges to effective integration	14
3.2.1. Biological response	15
3.2.1.1. Synaptic remodeling	16
3.2.1.2. Modulation of network activity	16
3.2.1.3. Remodeling of subtype-specific markers: excitatory (VGLUT1) and inhibitory (VGAT) synaptic markers	17
3.2.1.4. Effect on ion channel expression	17
3.2.2. Technical issues	18
4. Summary and organization of the Thesis	19
CHAPTER 2 MULTIUNIT ACTIVITY, LOCAL FIELD POTENTIAL, AND THE SPIKE TRIGGERED AVERAGE	20
1. What is Multiunit Activity?	21
1.1. Relationship between MUA and LFP	23
1.2. Results	24
1.3. Interpretation of results	25
2. What is Spike Triggered Average?	25
2.1. Steps of computation in the code used for spike triggered average	27
2.2. Results	30
2.3. Interpreting STA	33
2.4. Applications for future use	33
2.5. Disadvantage of using Spike triggered average	34
3. STA-LFP and LFP-MUA coherence	35
CHAPTER 3 SPIKE TRIGGERED COVARIANCE AND CORRELATION	36
1. What is Spike triggered Covariance-Correlation?	37
1.1. Covariance and Correlation Matrix	38
1.2. Spike triggered Covariance and Correlation	41

2. Results	42
2.1. Discussion and interpretation	45
3. Future use of STC as a tool	51
CHAPTER 4 CONCLUSION	52
APPENDICES	55
APPENDIX A: Coherence analysis	56
APPENDIX B: Local field potential-spike triggered average	59
APPENDIX C: Spike triggered covariance and correlation	67
REFERENCES	74

## LIST OF TABLES

Table 1. Major contributors influencing LFP [12]	6
Table 2. Examples of microelectrode arrays and their applications	14
Table 3. Covariance Matrix for cases in Fig. 28	47

## LIST OF FIGURES

Figure 1. The Figure shows an action potential recorded from a pyramidal neuron in the CA1 region of a rat hippocampus, illustrating commonly measured parameters [10]	2
Figure 2. (A) Basic subunit of Shaker B. Four of these subunits are assembled into a functional channel [11]. (B) a schematic view of the channel from the outside showing the assembled four subunits or domains (or subunits, in the case of potassium channels) [11]	4
Figure 3. (A) Example of a neuron with the structure for a closed field (B) Neuron structure that would generate an open field (bottom left to right) (C) Organization of neurons that would generate an open field (D) Organization of neurons that would generate a closed field [13]	9
Figure 4. (A) 8 * 8 Utah multielectrode array (B) Single electrode site in the Utah multielectrode array (C) Labelled diagram of single shank Michigan style probe (D) Single shank Michigan style probe [26]	13
Figure 5. Steps for computation of MUA [56]	22
Figure 6. Coherence plot between MUA and LFP	24
Figure 7. LFP in frequency domain	24
Figure 8. The waveform represents Local Field Potential and the vertical lines below it shows the spikes recorded simultaneously [59]	26
Figure 9. The black waveform is the LFP - STA waveform [59]	27
Figure 10. Steps of computation of LFP-STA	29
Figure 11. Shows the overlap of snippets used to construct the STA in Figure 12, the spike occurs at 0 msec	30
Figure 12. LFP-STA for the snippets in Figure 11	31
Figure 13. LFP-STA for a window size of 8 msec (4 msec on each side)	31
Figure 14. Shows the LFP-STA for a window size of 12 msec (6 msec on each side)	32
Figure 15. Shows the LFP-STA for a window size of 20 msec (10 msec on each side)	32
Figure 16. Covariance matrix for a microelectrode with 16 channels	40

Figure 17. Correlation matrix for the covariance matrix in Figure 16	40
Figure 18. The LFP Spike triggered average for the mentioned animal	42
Figure 19. Overlap of all the 194 LFP snippets used for construction of STA	43
Figure 20. LFP-STA Covariance Matrix	43
Figure 21. A contoured version of the LFP-STA covariance matrix in Figure 20	44
Figure 22. LFP-STA Correlation Matrix	44
Figure 23. Contoured version of the LFP-STA Correlation matrix in Figure 22	45
Figure 24. Different scenarios that can exist when covariance is calculated (A) close to zero phase shift, (B) A random phase shift $\alpha$ , (C) Close to 180 degrees phase shift	46
Figure 25. (A) LFP snippets from 66 to 70 with LFP-STA (B). LFP snippets from 101 to 105 with LFP-STA	48
Figure 26. (A) LFP snippets from 42 to 48 with LFP-STA (B). LFP snippets from 78 to 82 with LFP-STA	49

## CHAPTER 1

### INTRODUCTION

This thesis pertains to the development of new signal processing algorithms to understand the tissue response to implanted electrode arrays in the brain. In particular, these tools are incorporated into the data analysis to unmask the effects of synaptic remodeling [1], changes in local dendritic arbors, and alterations in intrinsic excitability surrounding devices on the recorded extracellular potential [2][3]. Many of the techniques described herein pertain to understanding the relationship between the recorded spikes of individual neurons (unit activity) and the activity of the broader synaptic network (the local field potential). A brief overview of neuronal structure and function is provided to provide context for the subsequent chapters, as well as a primer on implanted electrode arrays.

#### 1. Overview of neuronal structure and function

The brain is made up of individual nerve cells or neurons which are the basic functional cellular unit of the brain. The structure of a typical neuron includes projections which serve as the location of signal input and output (dendrites and axons, respectively). The fibrous structures known as dendrites, together known as the dendritic tree, are covered with even smaller structures known as spines. A single axon projects from the soma, and as it approaches its target (which can be other neurons, muscles or gland cells), it branches into a number of smaller axons known as terminals or knobs. These points of functional contacts are known as synapses, whereby an electrical signal in a neuron can be transmitted to a downstream target.

##### 1.1. Signal generation of a neuron

The action potential, or “spike,” is the fundamental signal of interest in neuronal electrophysiology. The signal is largely shaped by the intracellular influx of sodium ions followed

by the efflux of potassium ions (Figure 1). In 1952, Hodgkin and Huxley wrote a series of five papers [4][5][6][7][8] that described the seminal experiments they conducted to determine the laws that govern the movement of ions in a nerve cell during an action potential. The first paper examined the function of the neuron membrane under normal conditions and outlined the basic experimental method pervasive in each of their subsequent studies. The second paper examined the effects of changes in sodium concentration on the action potential as well as the resolution of the ionic current into sodium and potassium currents. The third paper examined the effect of sudden potential changes on the action potential (including the effect of sudden potential changes on the ionic conductance). The fourth paper outlined how the inactivation process reduces sodium permeability. The final paper put together all the information from the previous papers and turned them into a mathematical model.

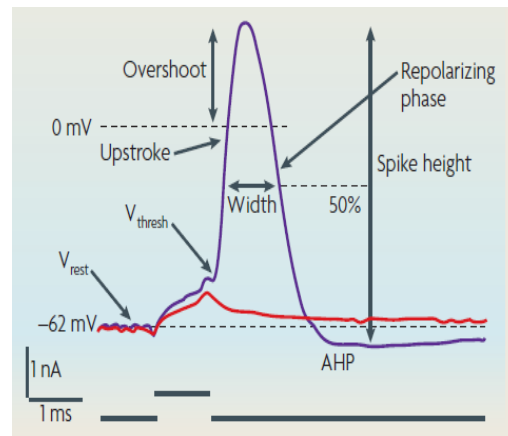


*Figure 1. The Figure shows an action potential recorded from a pyramidal neuron in the CA1 region of a rat hippocampus, illustrating commonly measured parameters [10]*

Critical to understanding the underpinnings of the action potential (AP) was the development of the voltage clamp, which uses an electronic device that allows control, or “clamping,” of membrane potential (V m) at a desired level. The difference between the measured variable and the set point creates an “error signal.” The error signal activates an effector system that decreases

the magnitude of the error. An amplifier measures the potential difference between an intracellular electrode ( $V_{in}$ ) and an extracellular electrode ( $V_{out}$ ). The output of this amplifier ( $V_m$ ) is the controlled variable and is compared with the command potential ( $V_{command}$ ), or set point, by an amplifier called the control amplifier. If  $V_m$  is not equal to  $V_{command}$ , an error signal causes a current to flow through an axial wire that is connected to the output of the control amplifier and inserted longitudinally through the axon. The current then flows out through the membrane to a grounded electrode to complete the circuit. The current passing through the axial wire rapidly and continuously causes  $V_m$  to remain equal to  $V_{command}$ . One way to measure the transmembrane current ( $I_m$ ) is simply to measure the current flowing out of the control amplifier.

The transmembrane currents are carried by ion channels embedded in the neuronal cell membrane, which are large macromolecular proteins that often consist of several peptide subunits. These channel proteins extend across the lipid bilayer and are in contact with the aqueous environment on both sides of the membrane. The channel protein forms a water-filled pore that allows ions to cross the membrane by electro-diffusion. Channels can open and close spontaneously and in response to various stimuli. Voltage-gated ion channels have an open probability (the fraction of time the channel is open) that depends on  $V_m$ . A typical  $Na^+$  voltage gated ion channel consists of a linear sequence of approximately 1800 amino acids. The  $\alpha$ -subunit contains all the functional characteristics of  $Na^+$  channels, including the pore-forming region and the voltage sensor. An  $\alpha$ -subunit contains four homologous domains (designated I, II, III, and IV), each with six  $\alpha$ -helical membrane-spanning segments (S1 to S6). Segment S4 has a positively charged amino acid at every third residue and is the voltage sensor [9]. A sequence of residues connecting S5 to S6 on the extracellular side of the channel, called the P region or P loop, dips partway into the membrane to form part of the channel pore. Figure 2 (A), shows a similar arrangement but in the case of

shaker B. K<sup>+</sup> channels are similarly structured, with the exception that four individual subunits (rather than domains) aggregate to form the tetrameric channel.

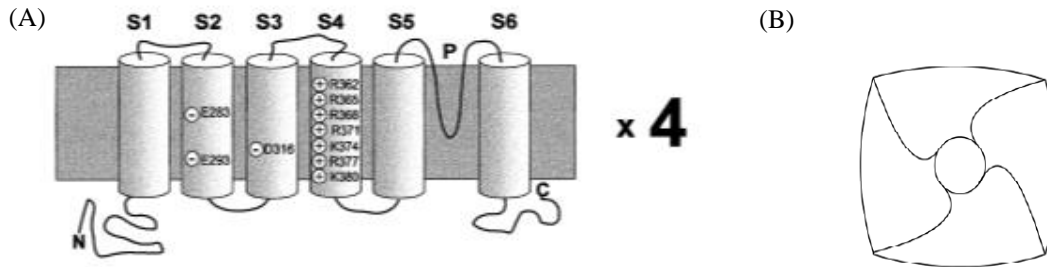


Figure 2. (A) Basic subunit of Shaker B. Four of these subunits are assembled into a functional channel [11]. (B) a schematic view of the channel from the outside showing the assembled four subunits or domains (or subunits, in the case of potassium channels) [11]

The four voltage-sensing domains (VSDs) from each S4 are arranged symmetrically around the central pore [11] as shown in Figure 2(B). At a negative  $V_m$ , S4 is electrostatically attracted to the inside of the membrane, and in that position it holds the channel pore in the closed configuration. Upon depolarization, S4 moves in the outward direction and may also rotate. That movement is coupled to the opening of the channel. The movement of charges on S4 generates a measurable current, known as the gating current.

## 1.2. Transmission of neuronal signals

Once the action potential is generated, how does the spread of electrical activity occur, and across what time course? The three passive membrane properties that are important to understand the spread of electrical activity are the membrane resistance, the membrane capacitance, and the internal resistance of long thin processes or cells. By modelling the membrane as an electrical circuit, the electrotonic potential can be analyzed. Many ion channels behave like conductors and can be modeled as a resistor, or conductor, with a single channel conductance,  $\gamma$ , when the channel is open. Most permeant ions are distributed asymmetrically across the plasma membrane. This

results in a chemical driving force that tends to push the ion through the open channel (E). This chemical force functions as a battery. Membranes usually contain several different types of ion channels that are each present in large numbers. In electrical terms, single channels in the membrane represent conductors arranged in parallel, i.e. the total conductance would be equal to the multiplication of,  $N_o$  (number of open ion channels), and the conductance of a single channel,  $\gamma$ . The lipid bilayer's ability to act as an electrical insulator makes it act like a capacitor ( $C_m$ ) connected in parallel with the elements representing the ion channels (the membrane capacitance). Membrane ionic currents cause  $V_m$  to change gradually, because of membrane capacitance. In response to a pulse of constant current,  $V_m$  follows an exponential time course to a new level. The time constant of this exponential curve is called the membrane time constant,  $\tau_m$ , and is equal to the membrane capacitance multiplied by the membrane resistance. The passive spread of small-amplitude, subthreshold signals along the surface of an axon is affected by membrane and axoplasmic resistances. The amplitude of these signals decreases as an exponential function of distance along the axon, which can be modeled by cable theory. The neuron makes efficient use of this mechanism in "saltatory conduction," which intersperses the active regeneration of the action potential at locations of highly concentrated voltage-gated sodium channel expression amongst intervening periods of passive propagation along the length of the axon. If the signal is successfully propagated to the synaptic terminal, transmission to a downstream neuron may occur through release of a neurotransmitter across the synaptic cleft. Neurotransmitters may have excitatory or inhibitory effects on the downstream neuron, depending on the nature of the receptor channels expressed in the post-synaptic membrane.

In a chemical synapse, the axon terminal is the top knob-like structure and the spine of the receiving neuron underlies it. There is a presence of a large number of vesicles clustered in the

presynaptic axon terminal. These vesicles contain chemical synaptic transmitters for a particular synapse. In between the pre- and post-synaptic terminals, there is a space known as synaptic cleft. When a synapse is active, the vesicles in the presynaptic terminal fuse with the presynaptic membrane and release their content of transmitter into the synaptic space. The transmitter molecules diffuse across the narrow synaptic space and attach to specific chemical receptors on the surface of the post-synaptic membrane, which activates the post-synaptic target cell.

2. Extracellular signal detection by implanted electrodes

Electric current contributions from all active cellular conductances within a volume of brain tissue superimpose at a given location in the extracellular medium and generate a potential,  $V_e$  (a scalar measured in Volts), with respect to a reference potential. The difference in  $V_e$  between two locations gives rise to an electric field (a vector whose amplitude is measured in Volts per distance) that is defined as the negative spatial gradient of  $V_e$ . The low frequency band of  $V_e$ , when recorded by a microelectrode in the brain, is referred to as the local field potential (LFP). The LFP is believed to primarily reflect the contributions of synaptic conductances within 100's of microns of the electrode site [12]. Other examples of contributors to the measured potential include sodium action potentials, calcium-mediated spikes, intrinsic currents and resonance, spike afterhyperpolarizations, and neuroglial interactions (Table 1).

Contributors to $V_e$	Description
Fast action Potentials ( $Na^+$ )	The strongest currents and can be detected as units, but still don't contribute to the LFP that much because the fields generated are of very short duration.

*Table 1. Major contributors influencing LFP [12]*

Table 1 (cont'd)

<p>Calcium spikes (Ca<sup>2+</sup>)</p>	<p>Long lasting (10-100 ms, amplitude varies from 10-50 mV) spikes can actively propagate within the cell and due to this their contribution to the LFP can be substantial</p>
<p>Intrinsic currents and resonance</p>	<p>Some neurons possess resonant properties i.e. when the intracellular depolarization is large enough, self-sustained oscillations are generated. For example: currents flowing through hyperpolarization de-inactivated cyclic nucleotide-gated channels (I-h) and low-threshold hyperpolarization-induced transient Ca<sup>2+</sup> currents, which often lead to burst firing (I-t) contribute to intrinsic resonance and self-sustained oscillations. Since resonant properties depend on both frequency and voltage, its impact varies with LFP in a complex manner.</p>
<p>Spike after polarizations and down states</p>	<p>Elevation of the intracellular concentration of a certain ion may trigger influx of other ions through activation of ligand-gated channels, and this will, in turn, contribute to LFP (the amplitude and duration of such burst-induced afterhyperpolarizations can be as large as synaptic events)</p>
<p>Gap Junctions and Neuroglia interactions</p>	<p>Direct electrical communication between neurons through gap junctions (also known as electrical ‘synapses’) can enhance neuronal synchrony; they also can affect neuronal excitability and contribute indirectly to the extracellular field.</p>

The signal that is detected from the electrode placed inside the brain is the summation of activities from all the sources listed in the table above and many other sources. In order to obtain

the LFP or the units/spikes, signal processing techniques are applied: a first step is to filter the signal into relevant frequency bands. For spiking activity, a high pass filter is applied at the desired range, which will attenuate all the frequency content less than that value. This high pass filtered signal can be further processed to obtain the spikes. Often, a threshold is set as several times the standard deviation above or below the mean of the signal to initially extract the spikes as threshold-crossing events. Principal component analysis can further distinguish individual spikes based on their similarity in waveform shape. Similarly, if we are interested in obtaining the LFP, which are slow travelling waves, a low pass filter is applied which attenuates all the high frequency content above a chosen value. Analyzing the LFP requires a broader understanding of the factors that influence it:

### 2.1 Neuronal geometry and architecture

Neuronal architecture and geometry influence the LFP significantly. For example, neurons that generate “open fields” make a sizeable contribution to the extracellular potential, whereas the neurons that generate “closed fields” do not [12]. This, in turn, depends on the distance between the current sources and the sinks (i.e., open conductances along the cell membrane), which is decided by the geometrical features of a neuron. Figure 3(A) shows an example of a neuron where the source and the sink are close together giving rise to a closed field, whereas Figure 3(B) shows a neuron where the source and the sink are at a larger distance (giving rise to an open field). The measured potential depends on how these neurons are arranged spatially in different regions, which can lead to synchronous superposition (e.g., in Figure 3(C) neurons lie parallel to each other, contributing significantly to LFP). A different arrangement might lead to the waves cancelling each other out (e.g., in Figure 3(D) the neurons individually generate open fields, but the way they are arranged gives rise to a closed field). In other words, a small LFP

amplitude could occur even when the magnitude of the population activity might be substantial, if the arrangement of neurons occurs in a manner similar to Figure 3(D). This is an important consideration when assessing LFP amplitude as a reflection of signal quality, and it also is relevant for understanding field contributions in the context of dendritic loss and remodeling surrounding implanted electrodes.

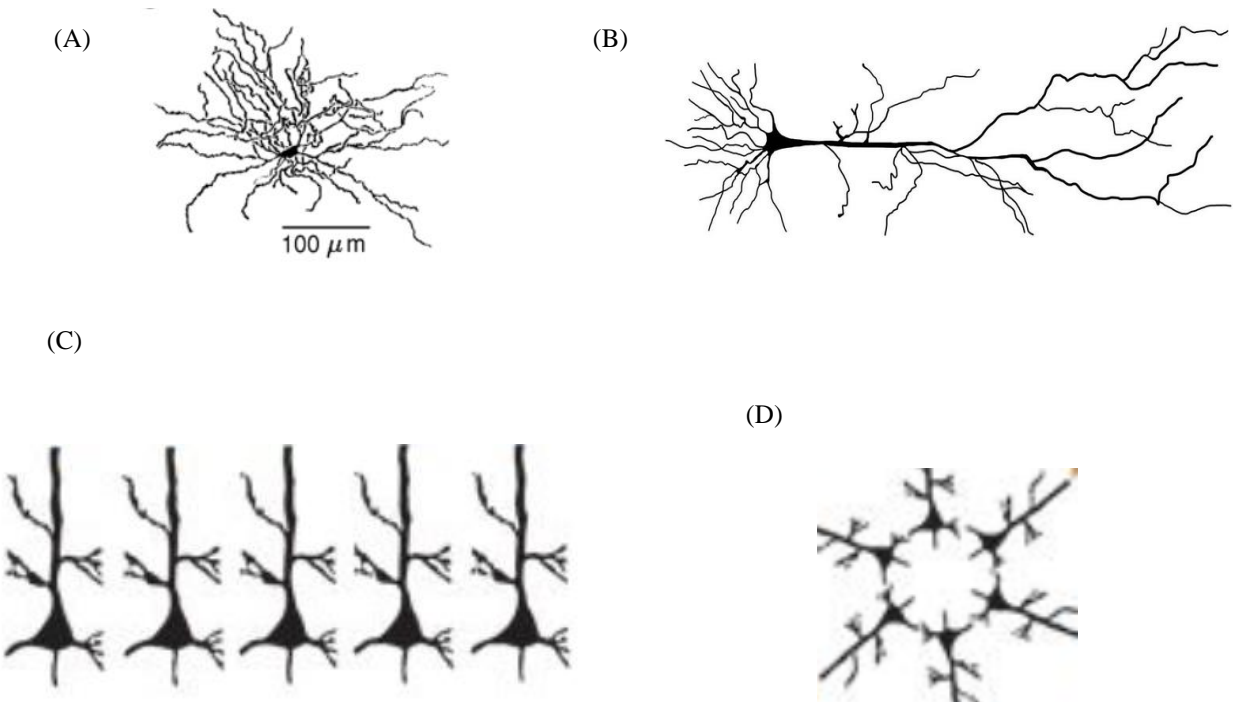


*Figure 3. (A) Example of a neuron with the structure for a closed field (B) Neuron structure that would generate an open field (bottom left to right) (C) Organization of neurons that would generate an open field (D) Organization of neurons that would generate a closed field [13]*

## 2.2 Temporal scaling properties

In addition to cytoarchitecture, a second critical factor in determining the magnitude of the extracellular current is the temporally synchronous fluctuations of the membrane potential in large neuronal aggregates. A quantitative feature of the LFP is that the magnitude of LFP power (that is, the square of the Fourier amplitude) is inversely related to temporal frequency  $f$ ; that is, there is  $1/f^n$  scaling (the exact value of  $n$  depends on various factors). There are several reasons that this might happen. One of them might be due to the low-pass frequency filtering property of dendrites [14], typically owing to a serial capacitance which depends on the distance between the soma and the location of the input, and on the membrane time constant. As the electrotonic length and input resistance of neurons can be effectively altered by synaptically induced excitatory and inhibitory conductance changes [15][16], the frequency filtering performance of neurons depends not only on the geometric characteristics of the neurons but also on their physiological state. Another reason is related to the capacitive nature of the extracellular medium itself [17],[18]. Network mechanisms also contribute to the  $1/f^n$  feature of the power spectrum [19]. In a brief time window, only a limited number of neurons can be recruited in a given volume, whereas in longer time windows, the activity of many more neurons can contribute to the LFP, therefore generating larger amplitude LFP at slower frequencies.

## 2.3 Role of volume conduction

The electric field specifies the forces acting upon a charged particle. The field is defined at every point of space from which one can measure a force 'felt' by an electric charge, and it can be transmitted through volume (for example, through brain tissue); a phenomenon known as volume conduction. In a volume, the  $V_e$  induced by a current dipole depends on the magnitude

and location of the current source, and on the conductivity of the extracellular medium. Conductivity in the medium depends on the degree of isotropy and homogeneity of the medium and is therefore a function of a number of factors, including the geometry of the extracellular space. The relationship between  $V_e$  and the current source density (CSD)  $J$  (measured in amperes per meter square) at a particular point of brain tissue is given by Maxwell's equations of electromagnetism. In their simplified form (that is, when the magnetic contributions can be neglected), these equations dictate that  $\nabla(\sigma \rightarrow V_e) = -\nabla J \rightarrow$ , where  $\sigma \rightarrow$  (amplitude measured in  $S\ m^{-1}$ ) is the extracellular conductivity tensor. The properties of  $\sigma \rightarrow$  crucially affect the waveform and functionality of the spatiotemporal  $V_e$  deflections. Measurements of the extracellular medium in the relevant frequency range ( $<10$  kHz) have not yet fully resolved this issue, with some experiments concluding that the extracellular medium is anisotropic and homogeneous[20],[21], and others suggesting that it is strongly anisotropic, inhomogeneous [22],[23] and may even possess capacitive features.

### 3 Implanted electrodes in the brain: Progress and challenges

A microelectrode is an extremely fine wire or microfabricated electrode that enables the measurement of the electrical potential following implantation into nervous tissue. In recent years, numerous fabrication strategies encompassing a wide range of materials and architectures have permeated the neural engineering field [24]. Historically, silicon microtechnology has been a mainstay approach to meet the demands of neural applications, allowing multiple functions to be integrated on a single implantable microsystem. Besides reproducibility and low variability of silicon-based microelectrodes, combination of various functionalities like standard electrophysiology, integrated signal processing, local drug delivery, neurochemical detection and optogenetic stimulation is also possible using these microsystems. This ability makes silicon

microelectrodes good candidates to provide high-resolution recording and stimulation in the electric, fluidic, chemical or optical domain in more complex neurophysiological experiments in the future [25].

### 3.1 Silicon based microelectrodes

Some of the most widely used silicon based microelectrodes are the Utah multielectrode array and Michigan style probes (Figure 4). The Utah array is a commercially available intracortical electrode array consisting of up to 100 silicon needle-shaped electrodes, which are produced via microscale fabrication techniques such as thermomigration, a combination of mechanical and chemical micromachining, metal deposition, and encapsulation with a polymer made of imide monomers. The Utah array enables users to acquire neural activity from different cortical areas. However, they are limited in their ability to target deep neural structures in the axial direction. This is where Michigan probes come into play where the electrode sites are laid across the shank and can be used to record from multiple layers at the target site. Michigan probes have been successfully used in several neuroscience applications, but they also suffer from some disadvantages related to limited thickness ( $>15$   $\mu\text{m}$ ) and length ( $<8$  mm). Nonetheless, these devices remain important tools in neurophysiology studies. Examples of the application of Michigan probes and Utah arrays are provided in Table 2.

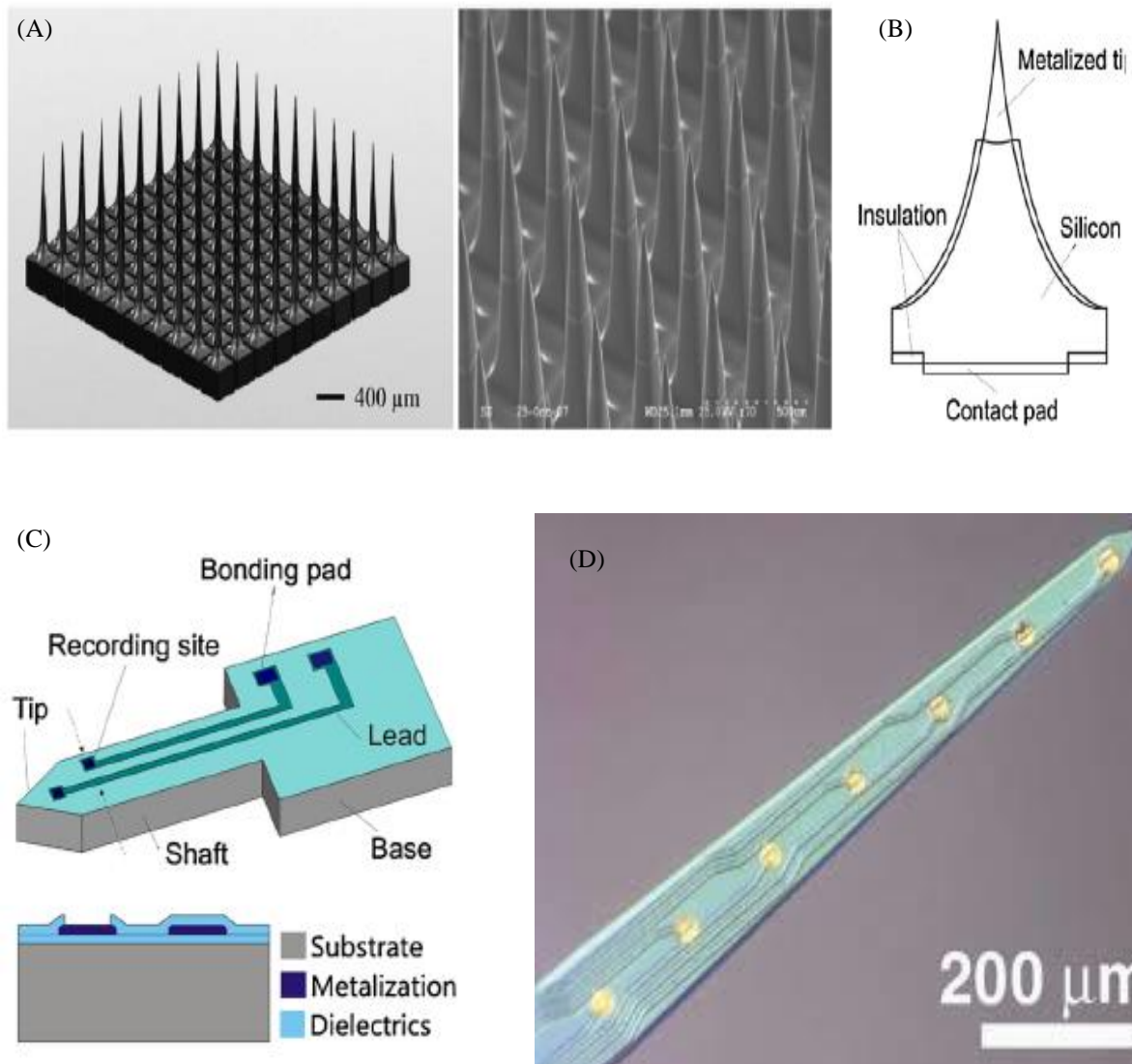


Figure 4. (A) 8 \* 8 Utah multielectrode array (B) Single electrode site in the Utah multielectrode array (C) Labelled diagram of single shank Michigan style probe (D) Single shank Michigan style probe [26]

<b>Multielectrode-Array (MEA)</b>	<b>Example Applications</b>
Utah multielectrode array	Neuroprosthetic arm control via cortical motor activity in rhesus monkeys ( <i>Macaca mulatta</i> ) using Utah arrays [27].
	Electrically stimulate the spinal-cord according to decoded neural signals from the Utah array in the motor cortex of monkeys [28].
	Induced tactile sensations in the hand via targeted neural stimulation with Utah arrays implanted in the somatosensory cortex, as illustrated in [29].
Michigan style probe	Investigated neural activity in the hindlimbs of rats with spinal cord injuries using a 16-channel Michigan probe and explored treatment methods based on neuro-stimulation [30].
	Investigated the use of a neural interfacing system to recover neural function after brain injuries in small animals (i.e. rats) demonstrating that the missing brain functions can be restored using a brain-machine-brain interface [31].

*Table 2 Examples of silicon microelectrode arrays and their applications.*

### 3.2 Challenges to effective integration

The probes we discussed above are useful in a wide array of applications and have been very useful, but an ongoing problem with these electrodes is that they often do not provide reliable recordings when implanted for long periods of time. Signal amplitudes vary on a daily basis

[32], which can lead to difficulties analyzing, decoding, and interpreting the signals recorded. There are a wide array of reasons why this may happen, but two major contributors are: (1) the biological response to the implantation of the device (neuronal and non-neuronal response), and (2) the technical issues that arise with implantation of the electrode (signal processing algorithms, electrical and mechanical failures).

### 3.2.1 Biological response

In terms of the biological response, work by Biran et. al, used neuronal loss and gliosis as parameters to investigate device integration as a function of distance using immunohistochemistry (33). Significant neuronal loss was observed at 4 weeks within the first 100um compared to stab control, which did not fully resolve until ~500um, and a significant loss of neurofilament extended out beyond 200um. Non-neuronal cells in the brain include specialized supportive cells (such as astrocytes, microglia, oligodendrocytes and NG2-glia) and neurovascular cells. Microglia are the resident macrophage cells of the brain, which initiate the foreign body response by the release of inflammatory factors. They rapidly react to inflammation in the central nervous system, leading to encapsulation of the device at the site. Astrocytes are activated by the microglial signaling and likewise contribute to the device encapsulation. The barrier nature of gliosis has traditionally been assessed through in vivo measurements of the impedance of the tissue/electrode interface and modelled using static circuit elements. However, the electrode/tissue interface, especially in the presence of reactive gliosis, cannot be fully defined by these traditional methods [34]. More specifically, the barrier nature of gliosis is reflected in models of the effective volume of tissue activated, where greater gliosis reduces the number of neurons stimulated. The stimulation paradigm affects the impact of the glial barrier: in constant-voltage stimulation,

voltage is controlled, and the actual current delivered to tissue varies as the tissue response evolves (increased impedance due to gliosis reduces the stimulation delivered). Meanwhile, the impact of glial encapsulation on the quality of signals recorded in vivo remains ill-defined. A few lines of indirect evidence support the idea that glial encapsulation acts as a barrier to signal detection by implanted electrodes. For instance, astrogliosis, as identified by increased glial fibrillary acidic protein (GFAP) immunoreactivity, was associated with reduced recording quality of Utah-style arrays implanted in the rat cortex in a study that investigated the relationship between histology and recording quality. Additional possible biological impacts to the local tissue are summarized below:

#### 3.2.1.1 Synaptic remodeling

Synaptic remodeling is largely affected by its neurochemical environment, which, in turn, is affected by the device implantation. Due to the electrode implantation, cellular membranes are punctured, and astrocytes and microglia are activated. This results in increase of neurotransmitters in the extracellular environment [34]. This increase in neurotransmitter leads to the creation of a gradient which may attract and reinforce gliosis [35][36]. There is also the evidence of increased markers of inhibitory synaptic transmission surrounding devices [1]. All of these changes in the surrounding environment of the implant have the potential to lessen the effect of stimulation and add noise to the recorded signal. Nonetheless, these adaptations may reduce the spread of excitotoxicity, neuronal loss and also the likelihood of excessive synchrony.

#### 3.2.1.2 Modulation of network activity

Interconnected astroglia are able to orchestrate synchrony through the integration of signaling within neuronal circuits and across functional regions of the brain [37]. The

stimulated actions of a single astrocyte could dictate functional consequences on an entire network of neurons [37]. Given evidence for astrocyte coordination of neuronal networks, reactive gliosis likely impacts not only the generation and transmission of action potentials between single neurons, but also the broader population of activity detected and stimulated by electrodes implanted in the brain.

#### 3.2.1.3 Remodeling of subtype-specific markers: excitatory (VGLUT1) and inhibitory (VGAT) synaptic markers

Neurons, astrocytes, and microglia each have multiple unique subtypes which may be affected by injury in different ways. Neural circuitry in the brain is complex, where individual cells may receive thousands of connections from other cells, and neurons contain a large diversity of form and function. In recent work from our lab [1], a progressive shift from VGLUT1 to VGAT predominance at the device interface was observed over time. The results indicate an overall “switching” of early interfacial excitation to a later elevation in inhibition.

#### 3.2.1.4 Effect on ion channel expression

Ion channel expression and function is highly dynamic and modulated by many factors [2], including changes to the surrounding environment caused by injury [38] and inflammation [39]. Channel modulation can impact not only the signal generation capabilities of single neurons, but also their frequencies, patterns, and waveform characteristics that underlie information encoding. Additional work from our lab [2] investigated four voltage-gated ion channels (Kv1.1, Kv4.3, Kv7.2, and Nav1.6) based on their roles in regulating action potential generation, firing patterns, and synaptic efficacy. To understand whether shifts in the expression of selected ion channels

occurs at the interface of implanted single-shank microelectrode arrays, quantitative immunohistochemistry was performed over 6 weeks (with time points at 1 day, 1 week and 6 weeks). These observations were analyzed based on their expression, both spatially and temporally. Based on the spatial expression, the results support a shift toward a decrease in sodium channel expression and an increase in potassium channel expression over the chronic 6-week time course. When the temporal expression was analyzed, the relative shift in “unit” region Nav1.6 expression elevation at 1 week to depression at 6 weeks, coupled with the sustained elevation in all Kv channels at both time points, indicates a temporal shift from hyper- to hypo-excitability within the recordable radius of the device.

### 3.2.2 Technical issues

While biological factors are important determinants of signal quality, non-biological contributors are also important to consider. Technical issues include poor signal detection due to problems with noise, signal processing techniques, and electrical and mechanical failures. Signal processing affects the signal based on the spike sorting algorithms used, the features used for classification of spikes, how that data is processed after spike sorting, what kind of model is being used and how reliable it is. For example, as discussed by Michelson et. al. [40], the accuracy of a machine learning decoder (MLD) depends upon the features that are used for decoding after spike sorting (e.g., PCA-based single unit activity, PCA-based multi-unit activity, or a constant threshold). Additional observations underscore how different signal processing techniques affect the data and the results [40]. Electrical and mechanical failure likewise can drastically affect the recording. For example, a sudden increase in impedance caused by lead breakage or electrode site delamination,

insulation failures which might result in a drastic decrease in impedance, [41][42] tissue-device mechanical mismatch, device variability due to subtle differences during the microfabrication process, and motion artifacts.

#### 4 Summary and organization of the Thesis

In this introductory chapter, we have reviewed the source of the signal we obtain for analysis and what features might be affecting the signal, which can inform our signal processing techniques. The second chapter introduces two tools for assessing the connectivity between neuronal spiking and the network activity, namely local field potential-spike triggered average (LFP-STA) and spectral coherence analysis for multiunit activity (MUA) and the LFP. We talk about computation of these two methods and how the results can be interpreted. The last part of the chapter discusses potential future applications of these tools. The third chapter introduces another tool, which works with LFP-STA, known as spike triggered covariance (STC). STC looks further into the STA and the non-linear features responsible for STA. In this chapter, we begin by describing how simple correlation and covariance can be interpreted, and then move towards how covariance and correlation matrix can be calculated for LFP-STA. We then propose the possible interpretations the results might point towards and then discuss additional potential applications this tool can be used for in the future. The concluding chapter briefly summarizes the work, and how the tools introduced in each chapter integrate to reveal the changes in the tissue response around the electrode, and how these tools could be improved further and used in conjunction with other analysis techniques to reveal even more features.

## CHAPTER 2

### MULTIUNIT ACTIVITY, LOCAL FIELD POTENTIAL AND THE SPIKE TRIGGERED

#### AVERAGE

The extracellular data recorded from the electrode can be processed and used to investigate how neurons behave as an assembly (LFP) or as single neurons (unit activity). Like the LFP, which represents the behavior of a neuronal population, multiunit activity (MUA) is yet another way to look at a neuronal population, but in a different way. Whereas the LFP is often viewed as representing the activity of the local neuronal assembly within the first ~300 microns of the electrode (and, predominantly, the synaptic conductances [12]), MUA is used to represent the superimposed activity of the individual neurons in a relatively smaller region around the electrode (~up to 100 microns). The computation performed by a neuron can be formulated as a combination of dimensional reduction in stimulus space and the nonlinearity inherent in a spiking output. White noise stimulus or spike triggered average (STA) is one of the tools used to understand which dimension in the stimulus space the neuron is more sensitive to. Likewise, for the spike triggered average of the local field potential (LFP-STA), it can reflect the coupling between individual neurons and the local network [43][44][45][46]. LFP-STA represents the average LFP waveform surrounding individual spiking events.

The earliest attempts at neural characterization, including classic electrophysiological experiments [47], presented the neural system with simple, highly stereotyped stimuli with one or at most a few free parameters; this makes it relatively straightforward to map the input-output relationship, or tuning curve, in terms of these parameters. While this approach has been invaluable and is still often used, it has the shortcoming of requiring a strong assumption about what the neuron is “looking for.” Building on this concept, white noise was used as an alternative stimulus, which

naturally contains “every” signal [48]. The stimulus feature best correlated with spiking is then the spike-triggered average (STA); that is, the average stimulus history preceding a spike [49] [50]. Spike triggered average is used for variety of applications. Some use it to study the stimulus right before the spike in order to understand the characteristics of what the waveform that makes the neuron spike is like with goals of creating a model mimicking the behaviour [51], some use it to study the relationship between spiking activity and the extracellular potential to understand the effects of membrane potential on extracellular data [52], and some studies employ it as a tool to study connectivity between different regions based on the increase or decrease in the value of STA for different regions [53]. In this chapter, we explore what the relationship between MUA and LFP tells us about connectivity within the network and how LFP-STA can also be used to reveal the connectivity within a network. While both of these relationships tell us similar things, they do so in unique ways and reveal different characteristics about network connectivity. As such, they are useful tools to complement our assessment of the impact of the tissue response on the quality of signals collected from implanted electrode arrays.

#### 1. What is Multiunit Activity?

Multiunit activity is used to represent the combined activity of neurons in the vicinity of the electrodes in the order of (~100 um). Unlike unit activity or LFP, the frequency content present in MUA isn't just above 500 Hz (high frequency components) or below 300 Hz (low frequency) respectively. It contains contains frequency content spanning the interim frequency range (i.e., 300-6000 Hz). Likewise, MUA does not require the additional signal processing steps required to discriminate individual unit waveforms through sorting algorithms (often, through the use of thresholding, principal component analysis, or wavelets) [54][55]. The flow chart below shows how MUA is calculated in the program used in the analysis [56]:

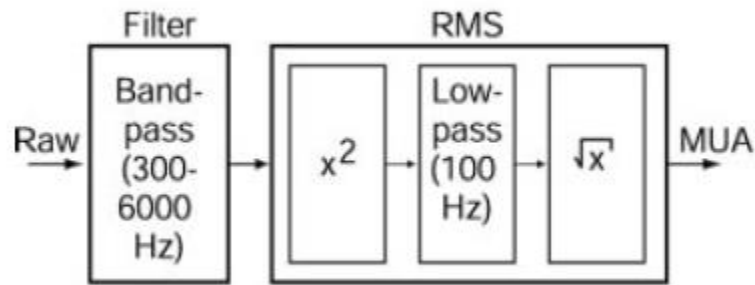


Figure 5. Steps for computation of MUA [56]

As seen from Figure 5, the frequency of MUA is between (300-6000 Hz). The (1/f) noise or pink noise is a signal with a power spectral density (energy or power per frequency interval) inversely proportional to the frequency of the signal. This makes the spiking activity (> 500 Hz) less prone to noise because it carries only high frequency content, and for this reason MUA is less affected by the noise. Additionally, since MUA does not require a thresholding step, its detection is less sensitive to underlying noise than unit detection. MUA also has been shown to have more independent features when looking at a particular brain area, because while the LFP (<300 Hz) at multiple electrodes tends to be highly correlated, comparatively little correlation exists in the MUA for the same recordings [56]. In the same study, the MUA predicted movement (reach and grasp) for a brain computer interface (BCI) with greater accuracy in comparison to the LFP and multiple spikes (MSPs). Apart from MUA being less affected by noise and having more features for characterization, an additional advantage in the context of BCI is that it can be used to replace the neuronal activity for decoding in a less computationally intense manner. BCI's that use sorted units for prediction require several computationally intense steps, which in turn requires more processing power and more complex circuitry. These factors might also lead to an increase in the

size of the device being used for decoding or limit wireless transmission; computation of MUA is an alternative, simplified way of assessing spiking activity.

### 1.1. Relationship between MUA and LFP

“Communication through coherence” is the notion that networks or neurons which have coherent electrical activity can communicate more effectively with each other[57]. In other words, neurons which fire in phase with one another will have greater functional connectivity and information transfer. In the case of the LFP, synaptic currents dominate; i.e., it represents the excitability of the broader neural network. The LFP generally can be regarded as the “input” to the system, and the local neuronal spiking as the downstream “output.” In a general sense, calculating the coherence of the MUA and LFP may reflect the communication strength between the local population of individual neurons within 100 microns of the device and the broader neural network. As such, the coherence may serve as an indicator of the level of neuron-network coupling. However, previous studies which calculated low coherence values between MUA and LFP suggest that this interpretation must be assessed carefully, as the relationship is likely to be complex and may require a more granular analysis within specific frequency bands [58].

We can perform the coherence analysis using equation 1 where  $F_a$  denotes the Fourier transform of (a), and  $S_a$  denotes the power in the frequency spectrum of (a). The numerator is the product of fourier transforms of MUA and LFP and the denominator is the product of power in the frequency spectrum of LFP and MUA:

$$Coherence_{MUA-LFP} = \frac{(F_{MUA} * F_{LFP}^*)}{(S_{MUA} * S_{LFP})^{1/2}} \quad \text{Equation 1}$$

## 1.2. Results

We perform coherence analysis using Equation 1 on recordings from the primary motor cortex in the right hemisphere of a rat, recorded by a 16 channel Michigan probe. The recordings used are part of a larger data set used in a previously published paper [2].

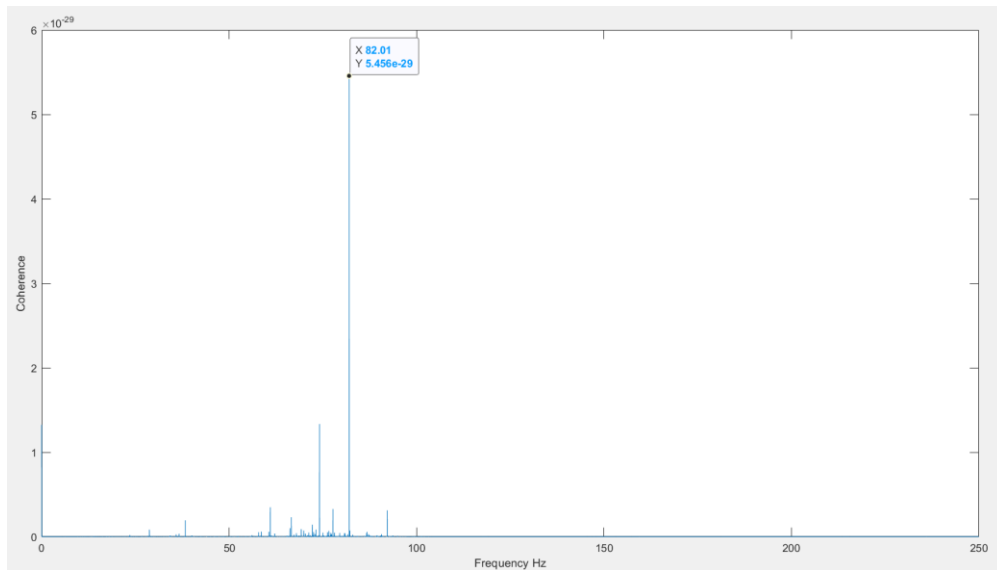


*Figure 6. Coherence plot between MUA and LFP*

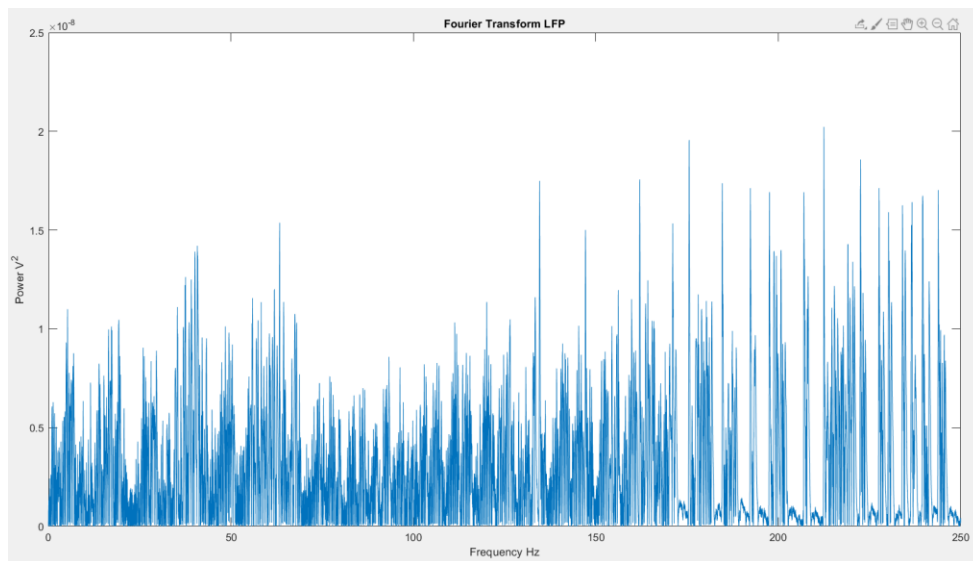


*Figure 7. LFP in frequency domain*

### 1.3. Interpretation of results

From Figure 6, we see that maximum coherence exists in the gamma band (20 Hz-90 Hz), and the maximum coherence exists at 82 Hz. This tells us that at that frequency there was the least phase difference between MUA and LFP, i.e maximum transfer of information occurs at that frequency. When coherence analysis is applied to the LFP and MUA, the frequencies over which the LFP and MUA have the least phase difference will reflect the frequencies at which the highest information transfer can occur (the frequency at which they lock with each other). We can then inspect the LFP power spectrum and determine the relative signal strength at that frequency (Figure 7), which might inform us about: (1) the strength of connectivity between MUA and LFP in that network, and (2) the amount of information transfer between LFP and MUA. As such, this calculation may contextualize parallel work in our lab which indicates decoupling of neurons from the broader network via image analysis of dendritic arbors and spines.

### 2. What is Spike Triggered Average?

An alternative approach to assess neuron-network coupling is through investigation of the spike triggered average of the LFP (LFP-STA). If we record spikes from a neuron (either intracellularly or via sorted units recorded extracellularly) and also record the local field potential near that neuron simultaneously, we can look at the relationship between these two recordings. In the LFP-STA, snippets of the LFP recorded within an affixed time window is centered at the timestamp of each detected spike, and the average of these snippets yields a final waveform known as the spike triggered average of the LFP.

A summary of the general computational process of the LFP-STA follows:

1. Once we have the LFP and spike data, the first step is to align them in the time domain and index the times at which we observe the spikes [59].

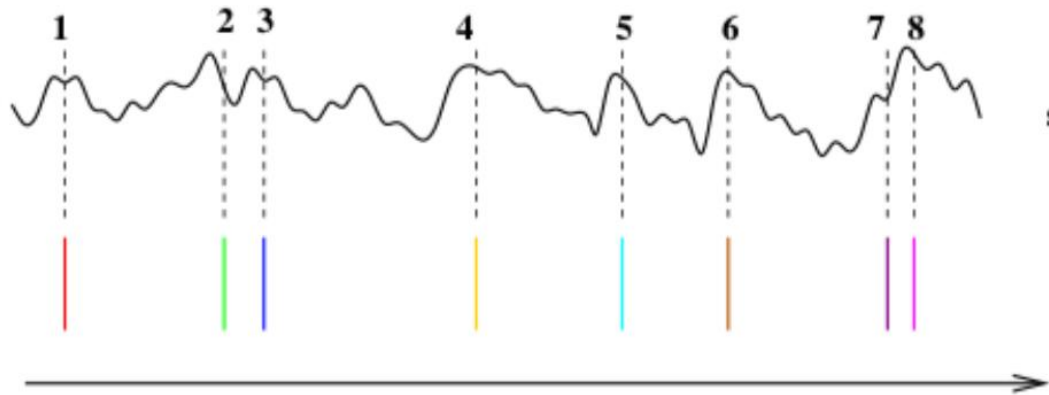


Figure 8. The waveform represents Local Field Potential and the vertical lines below it show the spikes recorded simultaneously [59]

2. After labelling these points on the extracellular waveform, we need to select the duration of the time window, which depends on various factors including the firing rate and the nature of the frequency response observed in the frequency domain.
3. Once we decide the size of this fixed time window, we need to determine what information we want out of the waveform. Are we interested in information just before the spike or information when the spike is happening? Based on the answer, in the first case, we take snippets from the extracellular waveform just before the time points recorded in the first step, or we place the window centered around the time point in the second case. Based on the results, we can see how the two responses are related in terms of phase (synchrony) and amplitude (strength of the response). In turn, this can yield new information on the relationship between individual neuronal spikes and the broader network activity [60][61].

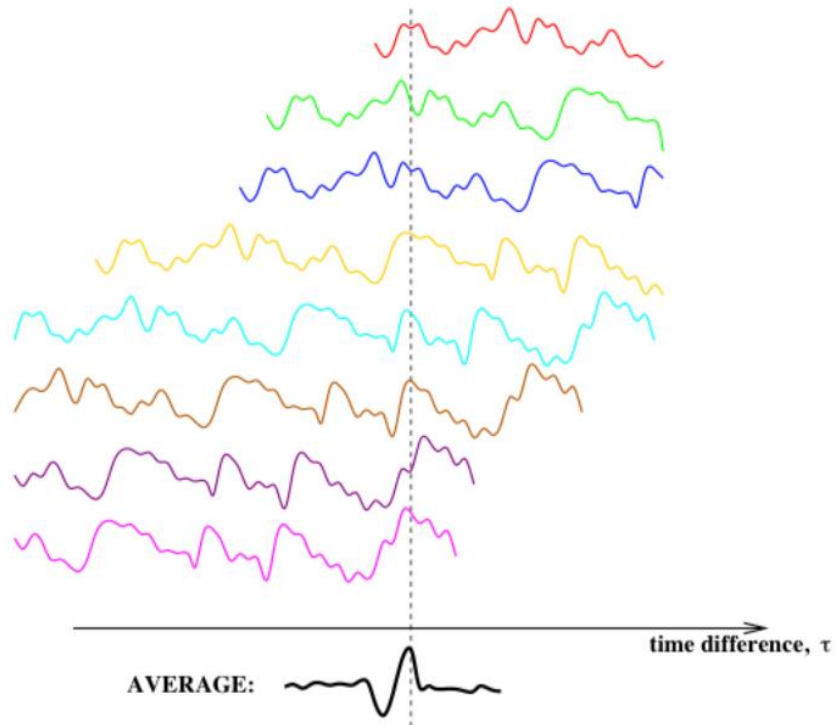


Figure 9. The black waveform is the LFP - STA waveform [59]

### 2.1. Steps of computation in the code used for spike triggered average

A brief summary of the code generated to calculate the LFP-STA is provided below. The MATLAB script is printed in Appendix A of this thesis. This code builds upon previous scripts used for LFP and spike sorting analysis [62][2]. The workflow is depicted in Figure 10.

- 1) The code needs two files to start running. The first file is the raw extracellular time series data and the second file has the information about the sorted units of the raw data obtained by processing the raw data through another program (TDT analysis). Once we have this data we can input them into the code.
- 2) The sorts file has a folder which contains the unit waveforms for every channel. This file is useful to see which channel has units and which just recorded noise as units. The TDT analysis code does this by high pass filtering the data at 500 Hz and creating a threshold.

The final step is applying principal component analysis (PCA) to the threshold crossings (2-3 msec snippets which are removed and stored), which clusters waveforms with similar shapes together for each channel, hence giving us the units waveforms. As desired, a final step involves visual inspection of the data to confirm legitimate unit waveforms. In the code written for LFP-STA in this chapter, we are processing all detected units irrespective of the waveform shape. In the future, we may analyze waveform shape manually or automate this process.

- 3) The second part of the code takes the LFP data files of the channels' raw data and applies a notch filter at 60 HZ to eliminate any contaminating hum noise. This information is stored in a separate matrix with respect to its channel until further use.
- 4) The third part of the code is used to index the time points at which these spikes occurred to mark those points in the LFP data and isolate a snippet of the desired duration second from that data centered around the time point. We do this by storing the time points at which spikes occurred in a different matrix for each of the channels. Next, we use these time points with respect to their channel and mark these time points on the LFP data acquired in second step. Once these time points are marked, a window is applied centered around that time point and that data is isolated. This is done for every spike in the channel, so in the end we will have a matrix of number of spikes, times the number of windows.
- 5) In the last part of the code we obtain the STA waveform. Each of the snippets obtained in the previous step are added together, and then divided by the number of spikes (hence, averaging the mean LFP waveform). Therefore, we obtain one STA waveform for each of the channels that were included in the processing after Step 2 for the recording time period of interest.

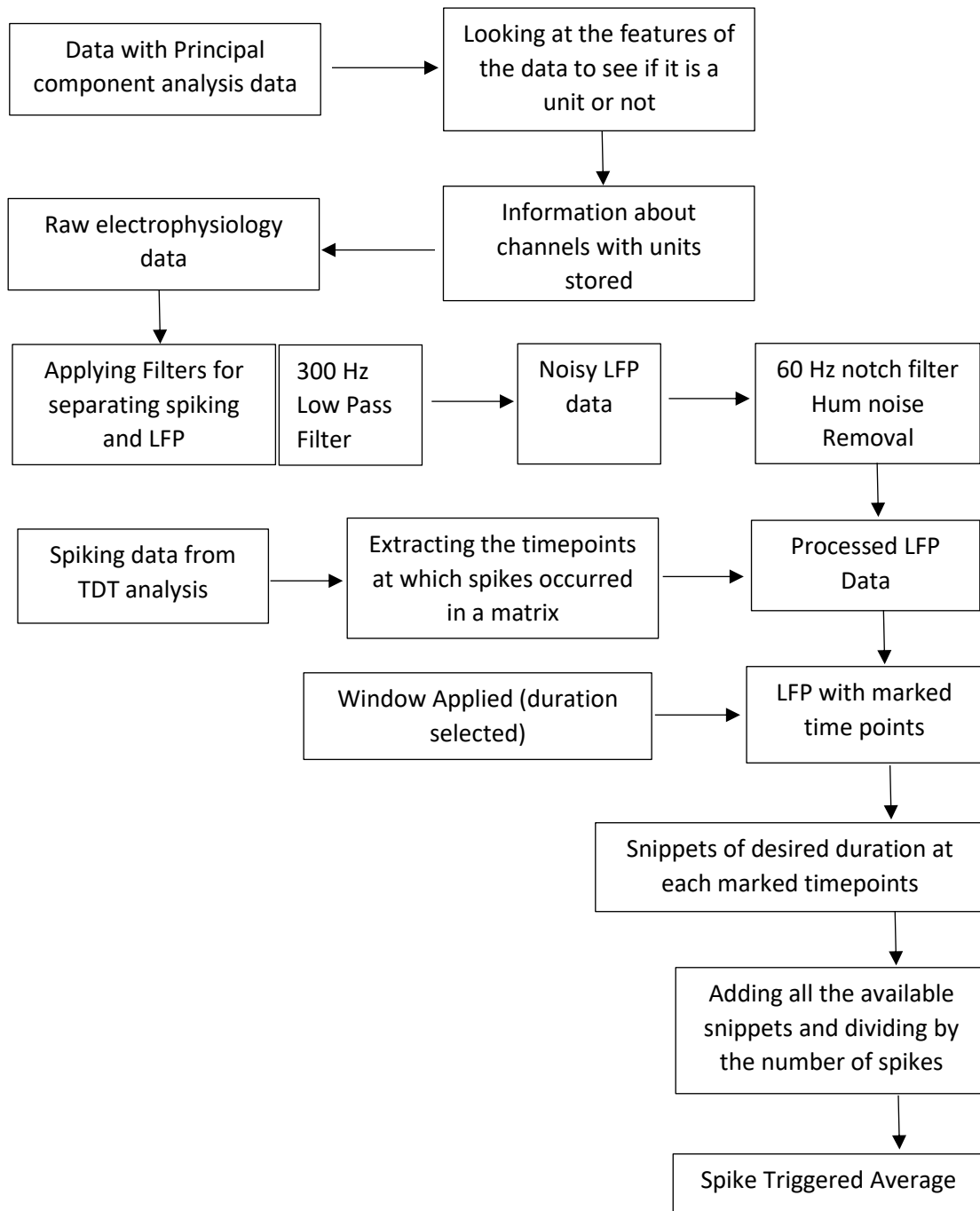


Figure 10. Steps of computation of LFP-STA

## 2.2. Results

Here, we look at the STA of recordings from the primary motor cortex in the right hemisphere of a rat, recorded by a 16 channel Michigan probe. The recordings used are part of a larger data set used in a previously published paper [2]. For the recording used in the following examples, the duration was 300 seconds with 194 spikes detected on the selected channel within that time. I have analyzed the STA for different window lengths (4, 8, 16, and 20 msec). The snippet overlap is only shown for a window of 4 msec (Figure 11). Widening the window was performed to visualize LFP modulation surrounding the spike occurrence over a broader time scale (thus capturing lower frequencies).

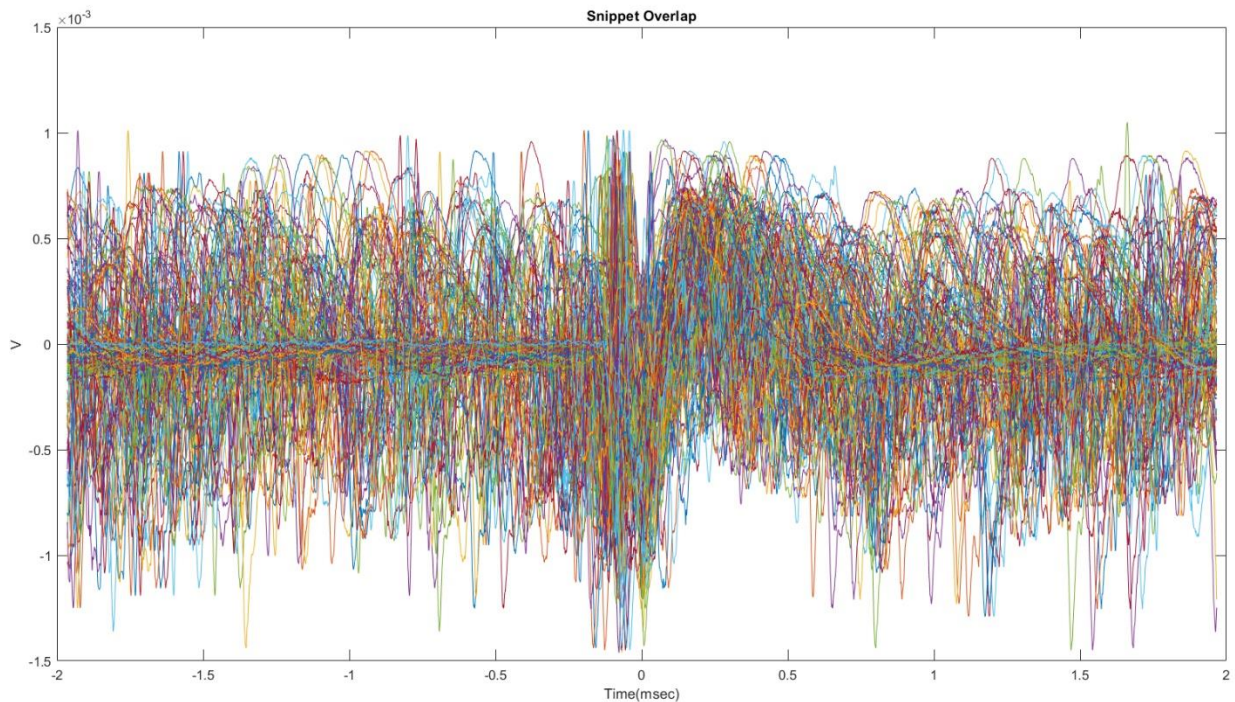


Figure 11. Shows the overlap of snippets used to construct the STA in Figure 12, the spike occurs at 0 msec

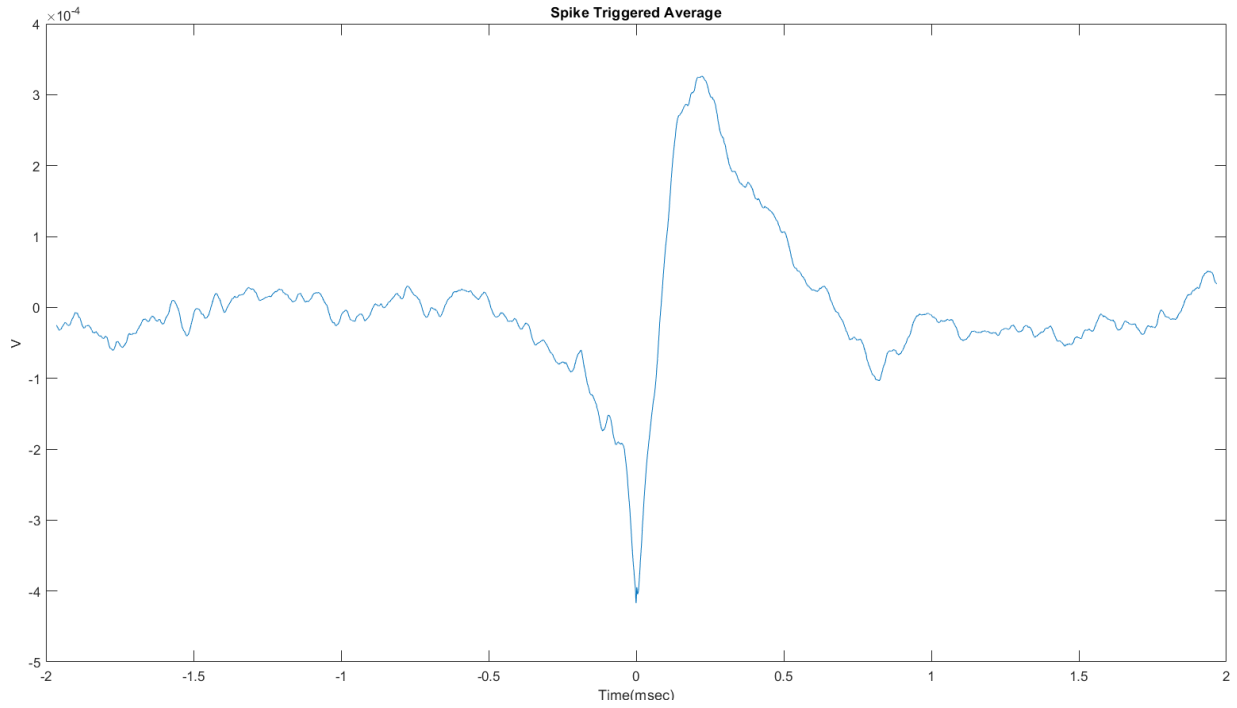


Figure 12. LFP-STA for the snippets in Figure 11

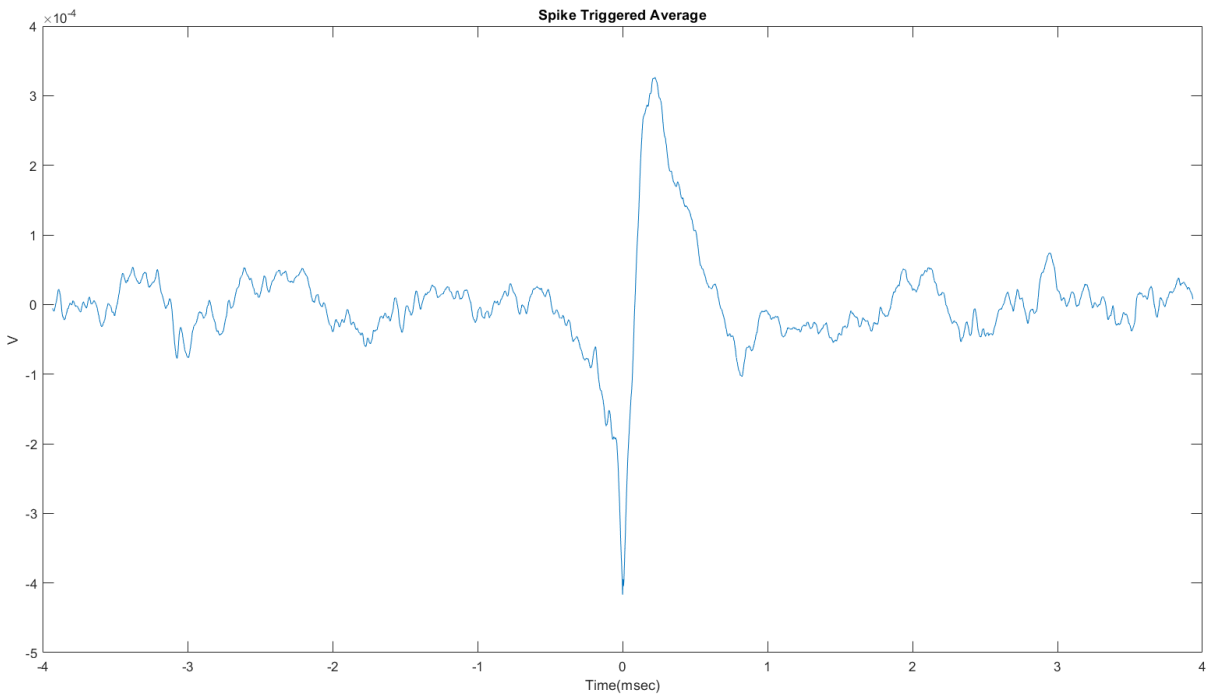


Figure 13. LFP-STA for a window size of 8 msec (4 msec on each side)

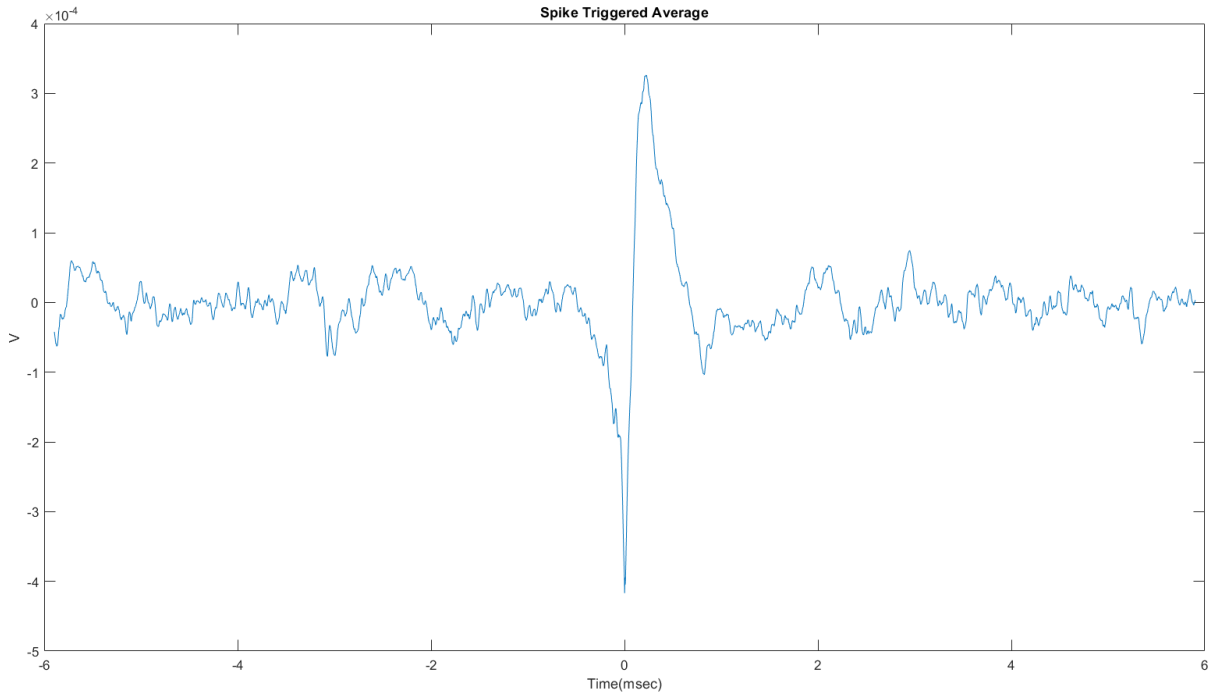


Figure 14. Shows the LFP-STA for a window size of 12 msec (6 msec on each side)

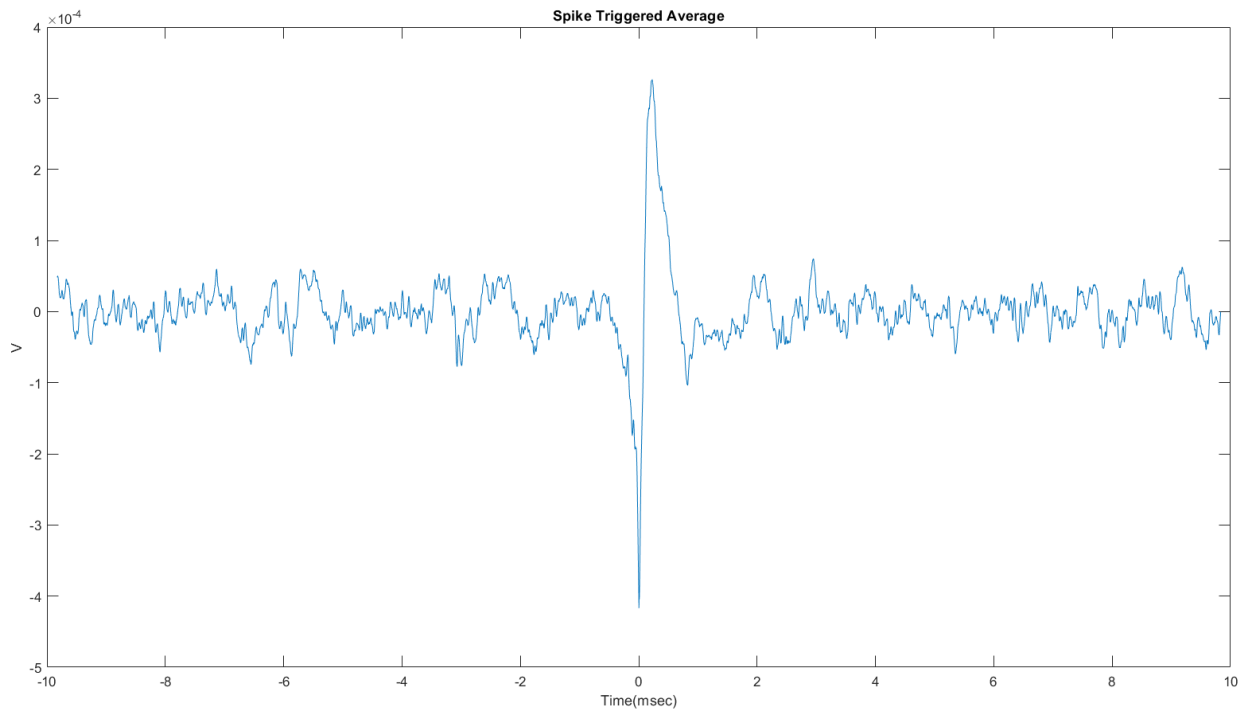


Figure 15. Shows the LFP-STA for a window size of 20 msec (10 msec on each side)

### 2.3. Interpreting STA

The spike triggered average of the LFP yields a visual representation of the relationship between the activity of individual neurons and the local field potential, i.e., single neuron activity with the local network. A large amplitude could reflect a high degree of coupling between the individual neurons and the local network activity. In the context of investigating the tissue response to implanted electrodes, this could reflect changes in local synaptic connectivity due to the presence of the device. Likewise, the STA also illustrates the phase shift between the spiking and LFP: does the spike occur on a relative up- or down-phase of the LFP? In summary, the STA can be used a tool to assess functional connectivity between the single unit activity and the LFP [63]. In turn, this may be an additional tool to assess structural remodeling in neurons surrounding implanted electrodes. Importantly, our recent observations suggest that neurons local to the device lose synaptic connectivity with the network over time.

### 2.4. Applications for future use

Additionally, there are multiple opportunities for new applications in future use:

- 1) Its use can be further extended if multiple microelectrodes or electrodes with multiple electrode sites are used; using the spiking activity at one electrode site as an index for LFP at another electrode site could deliver a map of functional connectivity between two regions. Also, when looking at the waveforms with one site as a spiking reference, we can look at phase differences between regions.
- 2) We can look at these waveforms across different time points to show how connectivity between regions changes due to the electrode implant. We might be able to assess the STA as a reflection of the morphological changes that are happening in the vicinity of the electrodes.

- 3) It can be used for assessing the effects of genetic knockdown delivered locally to the electrode, revealing even more specific relations and effects due to the neural implant. For instance, we may use the STA to assess the effects of knockdown of synaptic transporters or ion channels surrounding devices [1][2].
- 4) STA and current source density (CSD) analysis can be used together, which can give us a better picture into the composition of LFP in terms of contributions from different neural populations [64].
- 5) Another opportunity is to look at the spike-triggered average of the time–frequency spectrum of the LFP (STTFA), as used in [65]. Here, instead of averaging over segments of the LFP centered on each spike, the two-dimensional time–frequency energy plot of the LFP is averaged around each spike.

#### 2.5. Disadvantage of using Spike triggered average

The STA only provides us with the linear relationship between Spike-LFP activity and reveals nothing about the non-linear relationships between them. What this means is that when we look at the STA, it shows the average changes in the LFP at every spike for a given time window. As such, we lose information about the variation in the LFP snippets and the LFP waveforms that don't align with the average, which might otherwise reveal underlying structure in the data set. For instance, assessing the variation in the LFP snippets might reveal new observations that could reflect the underlying dynamics in neuron-network coupling, which could, in turn, be interpreted relative to structural and functional remodeling of neurons surrounding devices. This is a primary motivator for exploring the Spike-Triggered Covariance of the LFP (STC-LFP), in Chapter 3.

### 3. STA-LFP and LFP-MUA coherence

In summary, the LFP-STA is one tool to represent the relationship between neuronal spiking and network activity, where higher amplitudes may reflect greater coupling between individual neurons and the broader network. Likewise, the coherence of LFP-MUA may be interpreted similarly as representing the synchronization between LFP and MUA, which can be further assessed within specific frequency bands. As a complementary analysis to the STA, LFP-MUA coherence also provides us with added information on the frequency dependence of the relationship between spiking and network activity: does the communication between LFP and MUA increase in a certain band of frequencies? The combination of these tools may reveal new reflections of the tissue response in recorded extracellular electrophysiology data.

## Chapter 3

### SPIKE TRIGGERED COVARIANCE AND CORRELATION

In the previous chapter, we investigated the spike triggered local field potential average (LFP-STA) and how it can be used as a tool to understand and analyze the influence of neuronal spiking on network activity in different scenarios. However, the LFP-STA only reveals the linear characteristics of the neural response, while neurons exhibit other non-linear behaviors that are not revealed by the STA. In order to get a better understanding of these non-linearities, how they influence the neuronal response, and what this might reveal about the functional connectivity, we explored the use of spike triggered covariance of the LFP (LFP-STC).

Spike triggered covariance has been used to reveal highly complex modalities exhibited in the space of sensory stimuli. For instance, Schwartz et al. used STC to reveal and characterize a neuron model with gain control [66]. In a separate paper using non-centered spike triggered covariance, it was shown that neurotrophin-3 acts as a developmental regulator of receptive field properties in retinal ganglion cells [67]. STC also can be used to extract a low-dimensional subspace of the full stimulus space that is primarily responsible for generation of the neural response [68], including both excitatory and suppressive components in monkey V1. Spike triggered covariance takes STA a step further and is used to reveal the hidden and most relevant features of the stimuli that might be shaping the neuronal response, where that information may be used to characterize different non-linear behaviors by capturing those non-linearities in filters to recreate that neuronal response. In this chapter, we use spike triggered covariance and correlation in a novel application to explore what it may reveal about coupling between the single neuron (spiking activity) and local network activity (local field potential).

### 1. What is Spike triggered Covariance-Correlation?

Before describing Spike triggered Covariance or Correlation, we provide a brief review on how the simple covariance and correlation is calculated. For two variables X and Y, both with N number of elements, the following formula is used to find the covariance between these two variables (where  $\bar{X}$  and  $\bar{Y}$  are the mean of the X and Y respectively):

$$Cov(x, y) = \frac{\sum((X_N - \bar{X}) * (Y_N - \bar{Y}))}{N - 1} \quad \text{Equation 2}$$

So, every element in the array is subtracted with the mean for both the variables. The numerator in the equation is also known as the sum of cross products, where the elements of both arrays are multiplied elementwise (dot product) and then summed together. The last step is to divide this number by the degrees of freedom which in this case is N-1, giving us the covariance. The resulting covariance value, if positive, tells us that both the variables are increasing or decreasing together. If negative, it means that one of the variables is increasing and one of them is decreasing.

Now that we understand the covariance, we can look at how correlation is calculated. The equation to be used is as follows:

$$corr(x, y) = \frac{cov(x, y)}{\sigma(x) * \sigma(y)} \quad \text{Equation 3}$$

In Equation 3, the covariance between X and Y is divided by the product of their standard deviations denoted by  $\sigma(X)$  and  $\sigma(Y)$ . By doing this, the covariance between X and Y is standardized between 1 and -1 and is a dimensionless quantity. The correlation matrix, in addition to revealing positive or negative linear relationships, also reveals the strength of the relationship

between these variables. A value closer to (+1) reveals a stronger positive correlation whereas a value closer to (-1) reveals a strong negative correlation.

### 1.1. Covariance and Correlation Matrix

Covariance and correlation between two variables results in a single value which describes the linear relationship and strength of the relationship between them. But what if we want to look at the covariance between the recordings from various channels of a microelectrode? This is where covariance matrix becomes useful. Let's take a general example where we want to look at covariance between M channels with N time points, i.e. a N x M matrix. We use the following formula to calculate the covariance matrix,

$$\text{Covariance matrix} = \frac{\sum((M_N - \overline{M}_l) * (M_N - \overline{M}_l)^T)}{N - 1} \quad \text{Equation 4}$$

In the above equation, l is used to index the  $M^{th}$  channel and  $\overline{M}_l$  is the mean of that channel. In the numerator, every element in the  $M^{th}$  channel is subtracted by its mean and multiplied by the transpose of the same. These values are then summed and divided by N-1. This operation gives rise to a square matrix of M x M, where each value in the matrix corresponds to the covariance between those two channels. For example, (1,2) will reveal the covariance between channel 1 and channel 2. Also, this covariance matrix is a symmetric matrix; i.e., the values above and below the matrix diagonal are exactly the same. And the diagonal of this matrix is nothing but the covariance with itself which is the variance, so the values at (1,1), (2,2)...(M,M) are the variance values for each channel with STA as the mean.

Now let's look at the correlation matrix, which is derived in the same way as before by dividing the covariance values in the matrix by the product of its corresponding standard deviations.

The equation to be used is as follows:

$$\text{Correlation matrix} = \frac{\text{Covariance matrix}}{\sigma(M_i) * \sigma(M_i)} \quad \text{Equation 5}$$

This matrix, like the covariance matrix, is a square and symmetric matrix, where the diagonal values are all ones because we are dividing the variance by variance (product of standard deviations of the channels we are looking at the correlation of). This matrix, in addition to the direction of linear relationship, will also give the strength of the relationship between these channels.

While the downstream purpose of exploring the use of covariance and correlation matrices is to apply it on LFP-STA to reveal hidden effects of the tissue response on the extracellular signal, looking at the simpler example of the relationship between channels is provided as a starting point to illustrate what a covariance and correlation matrix can reveal about the data. As such, I have created the covariance and correlation matrix for data from a 16 channel, Michigan-style single-shank probe one day after insertion into the right hemisphere of the primary motor cortex of a rat. Each recording consists of 917248 samples collected at a sampling rate of 48828 Hz [2]. Below are 2 images which show a color plot of a covariance and correlation matrix across the 16 channels:

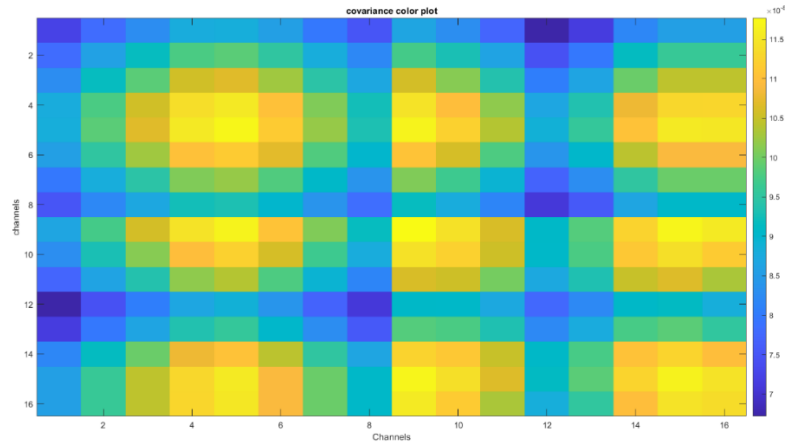


Figure 16. Covariance matrix for a microelectrode with 16 channels

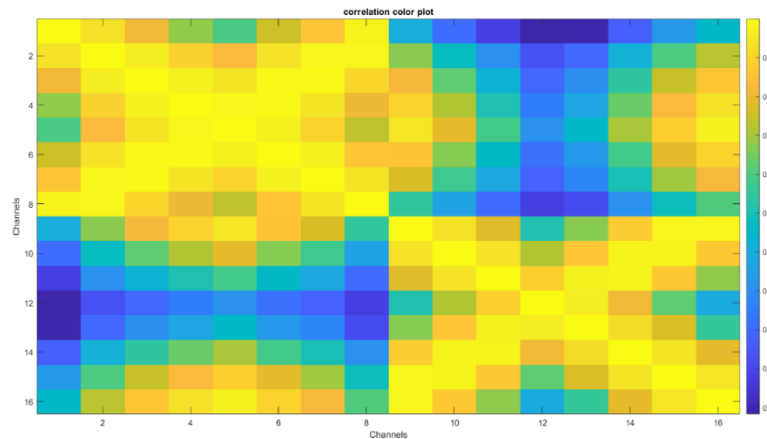


Figure 17. Correlation matrix for the covariance matrix in Figure 16

The result is a 16 x 16 symmetric matrix, where each element in the covariance matrix is a covariance between the corresponding channel. As the color bar shows, the highest values are represented by yellow and lowest by blue. Looking at the covariance matrix, we see that there is an increase and decrease in covariance across a group of channels at the same time. This might be showing the oscillatory behavior of the LFP, i.e. the up and down cycles of the LFP related to excitation and inhibition in the network. Inspection of the correlation matrix confirms that the diagonal is all yellow (i.e., +1), as expected. The remaining values between

(+1) and (-1) indicate how strong the correlation is between pairs of channels and not just their linear relationship. We see that the correlation values are high for several channels, which makes sense because the LFP recorded on nearby electrodes is expected to be highly correlated.

## 1.2. Spike triggered Covariance and Correlation

Building on how covariance and correlation matrices can be used together as tools, we can apply these methods to the LFP-STA. The spike triggered covariance matrix is a covariance matrix constructed by using the LFP snippets ( $S_N$ ) that were averaged to obtain the LFP-STA as elements of a matrix, where the mean is the STA itself and N is the number of spikes (or the number of snippets). Using Equation 4 for obtaining the covariance matrix, where every element is a LFP-snippet and the mean is the STA, is shown below:

$$STA \text{ Covariance matrix} = \frac{\sum((S_N - STA) * (S_N - STA)^T)}{N - 1} \quad \text{Equation 6}$$

Having calculated the LFP-STC, we can create the correlation matrix by using Equation 4.

Here, the covariance matrix is replaced with the matrix obtained in Equation 4, and the product of the standard deviation will be the standard deviations of the corresponding LFP-snippets used:

$$STA \text{ Correlation matrix} = \frac{STA \text{ covariance matrix}}{\sigma(S_N) * \sigma(S_N)} \quad \text{Equation 7}$$

## 2. Results

As proof-of-principle, I have calculated the LFP-STC and correlation matrix for the data from a single channel of a 16 channel Michigan-style single-shank probe one day after insertion into the right hemisphere of the primary motor cortex of a rat. The total recording time was ~300 seconds within which 195 spikes were recorded. The data used was down sampled, and the new sampling rate is 3051.8 Hz for the LFP.

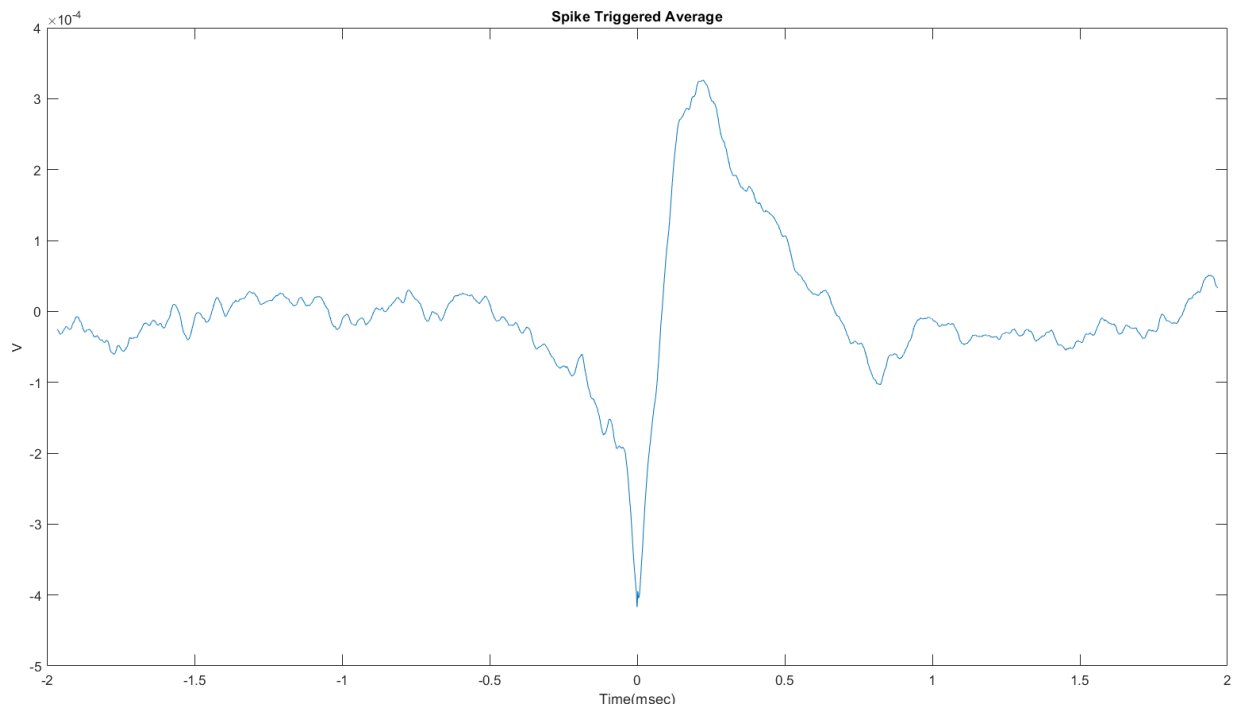


*Figure 18. The LFP Spike triggered average for the mentioned animal*

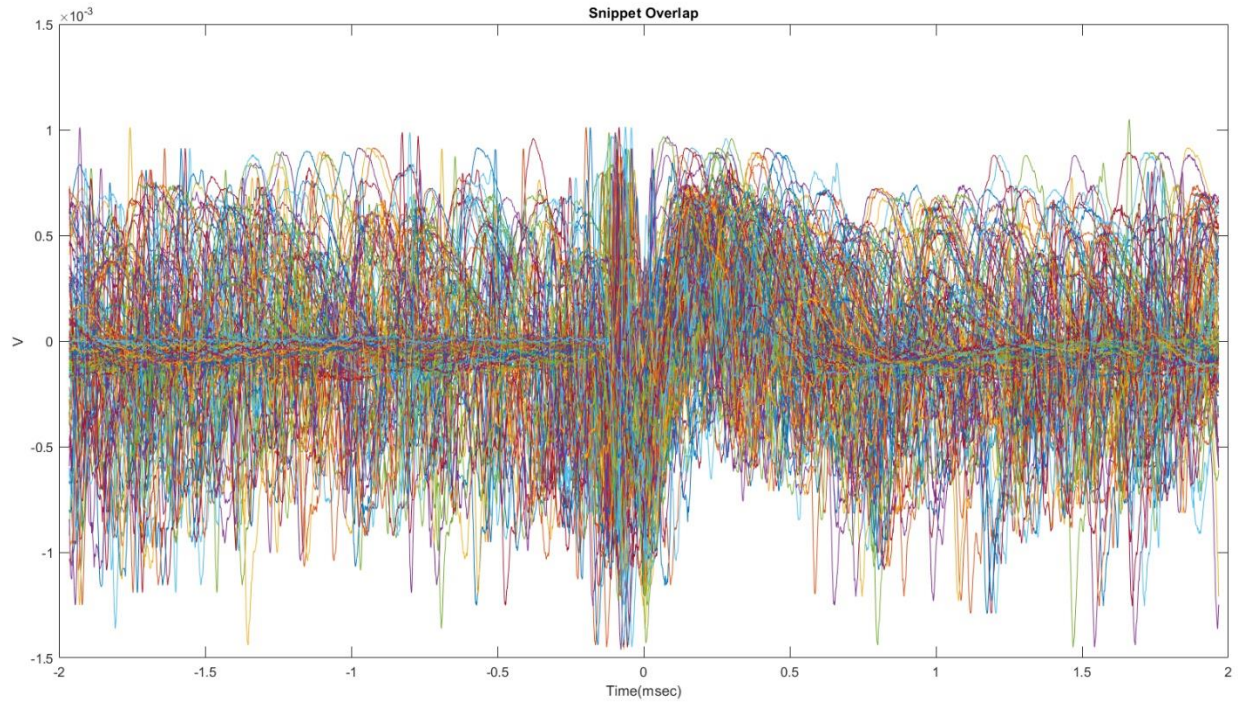


Figure 19. Overlap of all the 194 LFP snippets used for construction of STA

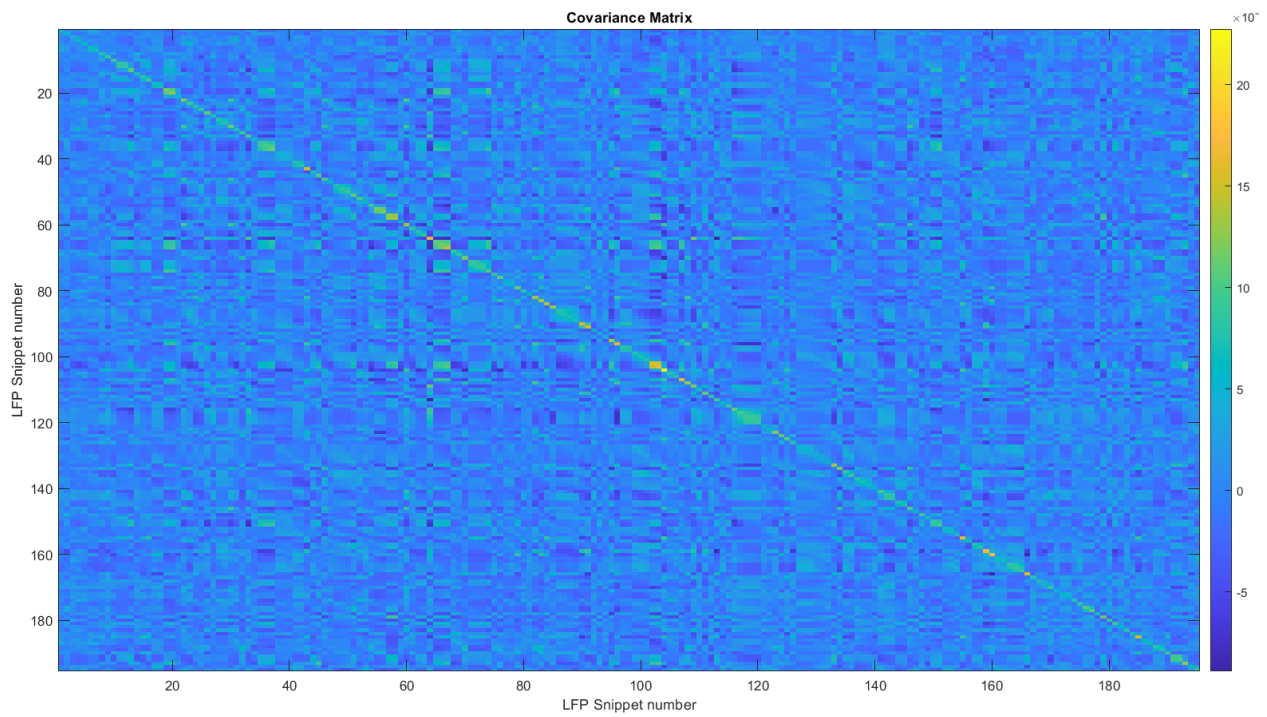


Figure 20. LFP-STA Covariance Matrix

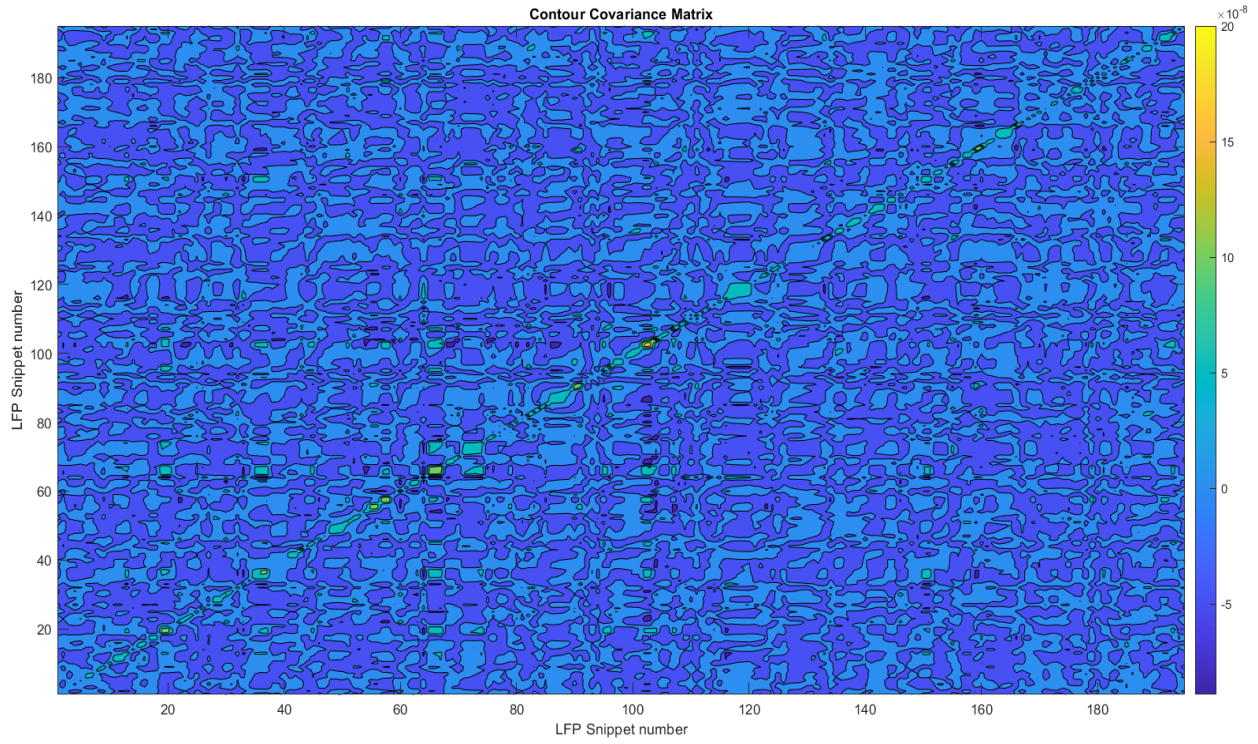


Figure 21. A contoured version of the LFP-STA covariance matrix in Figure 24

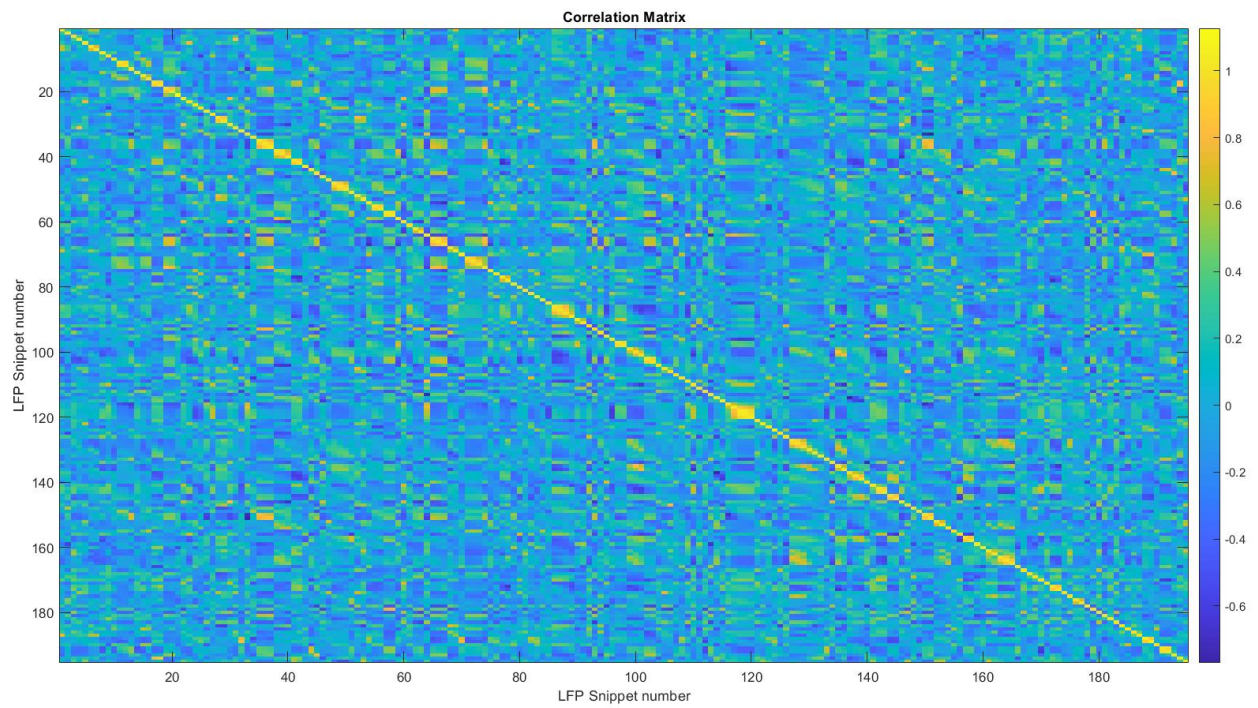


Figure 22. LFP-STA Correlation Matrix

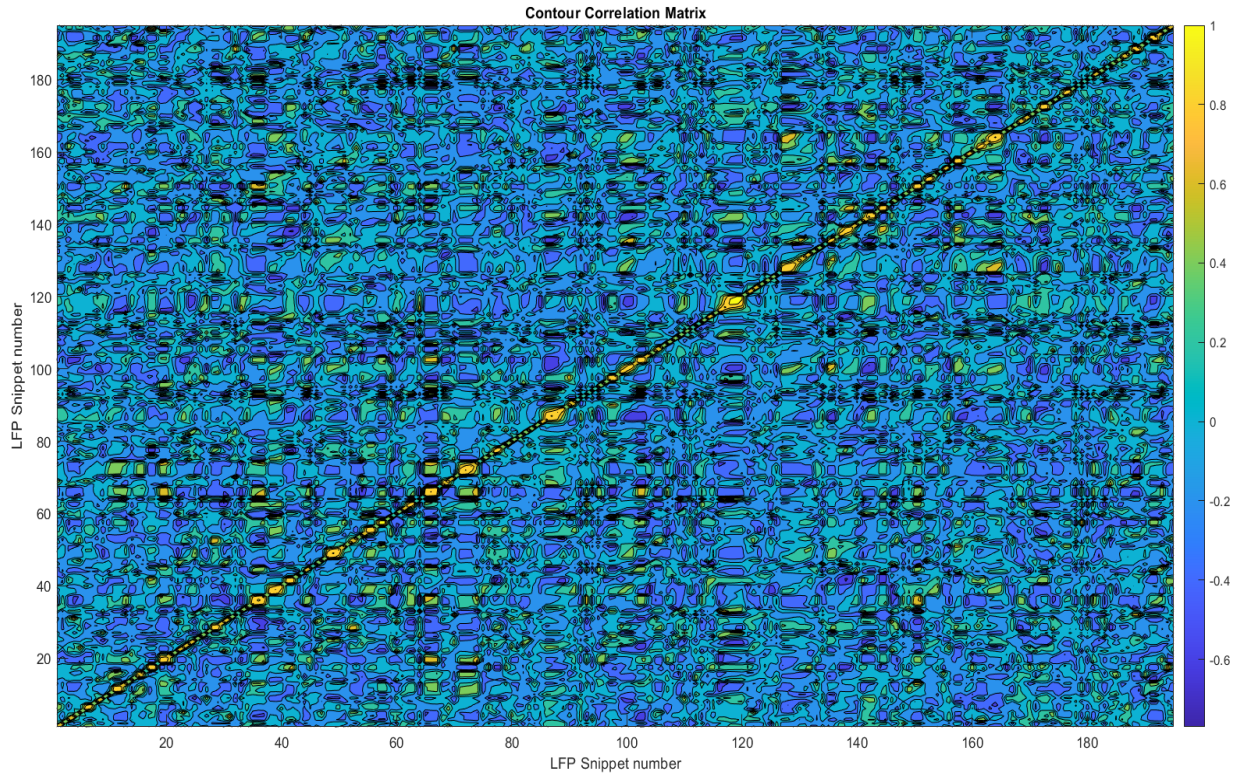


Figure 23. Contoured version of the LFP-STA Correlation matrix in Fig. 26

## 2.1. Discussion and interpretation

In the covariance matrix, every LFP-snippet is subtracted by the STA(mean), thus reflecting how different the LFP snippet is from the STA. In other words, the covariance matrix illustrates the similarity between the mean subtracted waveforms to each other (how similar they are to each other in terms of their difference from the STA). There can be three kinds of waveforms after the STA is subtracted from the snippet. In order to illustrate key concepts, Figure 24 shows artificially generated, phase-shifted sine waves to represent the three scenarios which may result in different covariance values. First, the snippet may have close to a zero phase shift (Figure 24(A)) and the mean subtraction results in a waveform which has a value close to zero across time. With these kinds of waveforms, the covariance will be higher with the snippets which have a similar relation with the STA (i.e.  $\sim 0$  phase

shift). The second scenario is when there is a random phase shift with the STA (Figure 24(B)). In this case, the covariance will be high between the snippets which have similar phase shift between them (i.e.,  $\sim x$  phase shift). The third type is when the snippet is almost completely out of phase with the STA (Figure 24(C)), which also results in a waveform which has values close to zero. In this case, the snippet is “working against” the STA waveform, but it will still show a high covariance, albeit with an opposing effect on the formation of STA waveform.

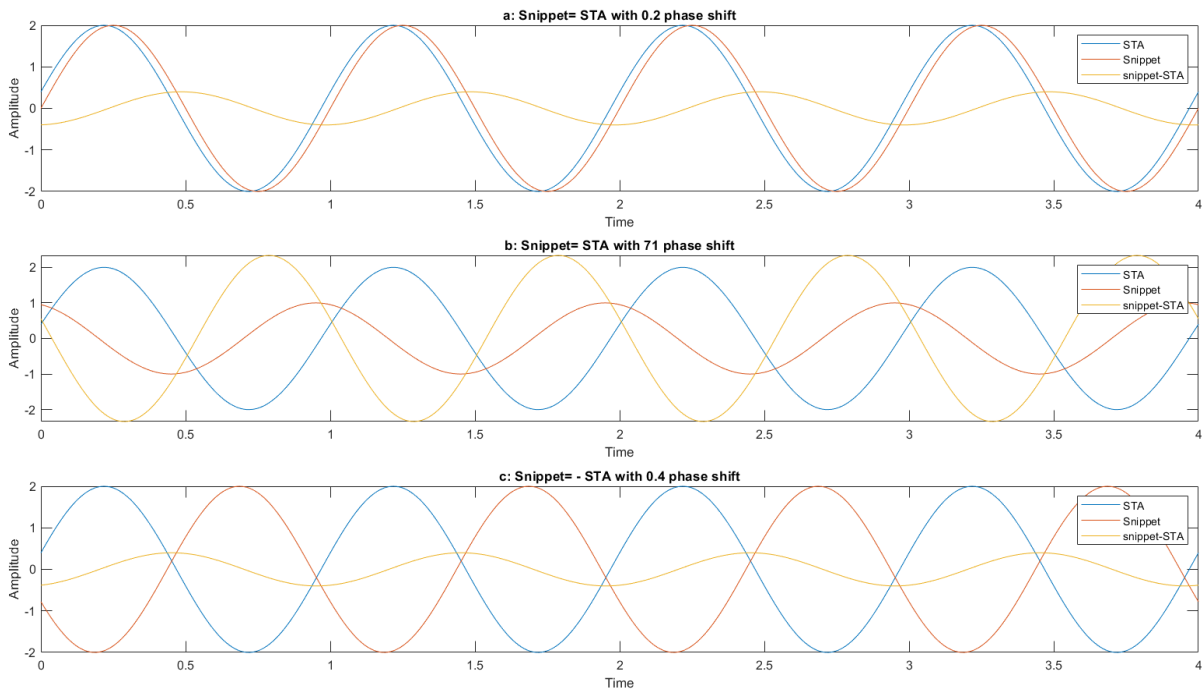


Figure 24. Different scenarios that can exist when covariance is calculated (A) close to zero phase shift, (B) A random phase shift  $x$ , (C) Close to 180 degrees phase shift

	1	2	3
1	0.0801	-0.155	0.159
2	-0.155	2.726	3.986
3	0.159	3.986	7.923

*Table 3. Covariance Matrix for cases in Fig. 24*

Table 3 shows the covariance matrix for the cases (A),(B) and (C), where (1,1) is the variance of (A), (2,2) is the variance of (B) and (3,3) is the variance of (C). And we see that the value at (A,A) has the least covariance which makes sense because it has close to zero phase shift, it increases at (2,2) and the variance is highest at (3,3) which also makes sense because the phase shift is close to 180 degrees. But when we look at the value at (1,3) it shows positive covariance, even though their contribution to the STA is the opposite.

In practice, when the covariance matrix of real data is calculated, the cases will not be as extreme. The diagonal of the covariance matrix becomes useful for interpretation (which, as discussed before, is the variance for each snippet). So, let's look at what different values of variance mean for the STA. The higher the variance, the more different the snippet is from the STA waveform. For example in Fig. 6, between (100-105, 100-105), we can see a yellow portion telling us that those LFP-snippets have a very different shape from the STA, similarly between (65-70,65-70), we can see green pixels again showing that there is a significant variance when compared to the STA. At all the other places in the diagonal we can see that the pixels are blue telling us that the variance is low and they must be positively affecting the shape of the STA. Figure 25 plots the snippets at those spike indexes, which indeed show high variance in comparison with the STA.

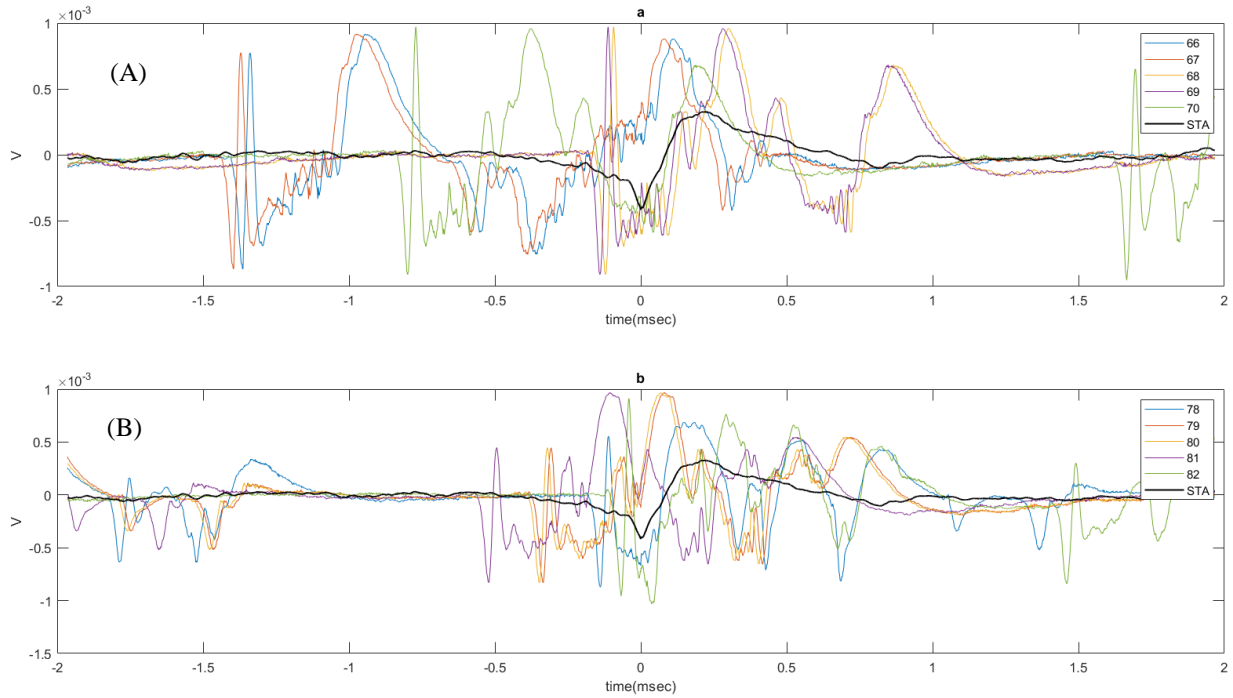


Figure 25. (A) LFP snippets from 66 to 70 with LFP-STA (B). LFP snippets from 101 to 105 with LFP-STA

Alternatively, in Figure 26, we look at snippets that have low variance with the STA. From the covariance matrix, we can identify regions of low variance between (40-50,40-50) and between (78-82,78-82). In Figure 26, we can see that at 0 msec (the spike time) all of the LFP snippets follow the trajectory of the STA, hence further reinforcing the interpretation of high or low variance values can be interpreted in terms of the similarity of individual LFP snippets with the STA.

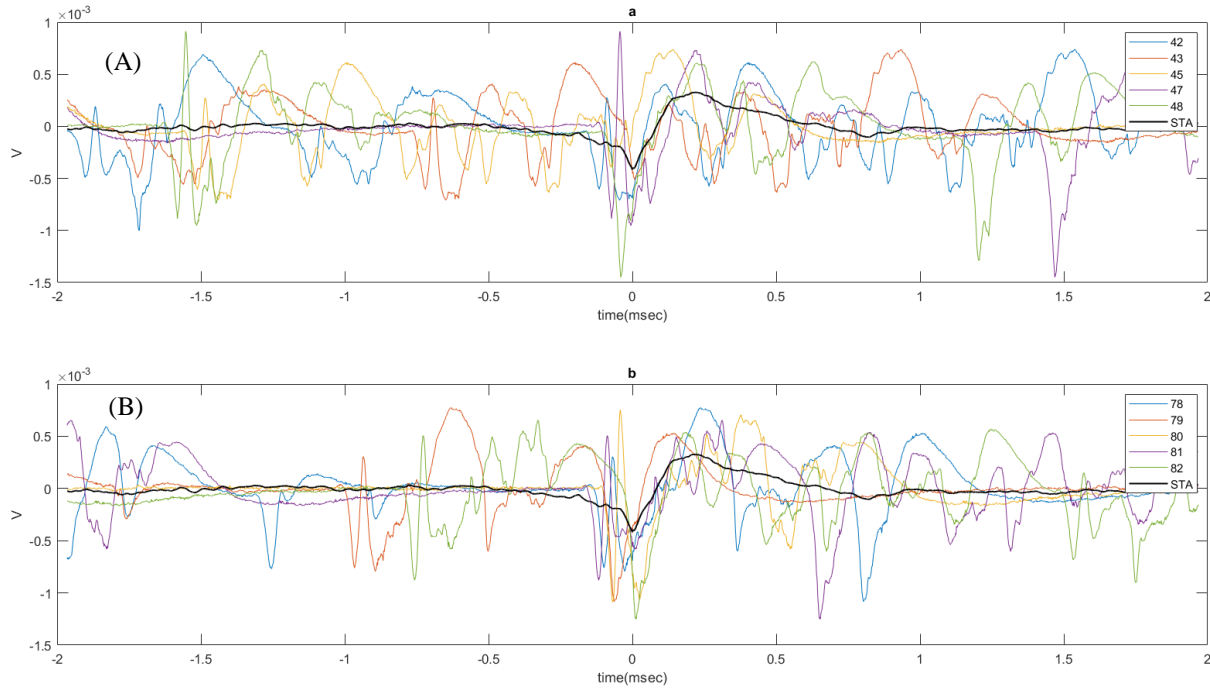


Figure 26. (A) LFP snippets from 42 to 48 with LFP-STA (B). LFP snippets from 78 to 82 with LFP-STA

Now that we know which values have a positive and negative variance with respect to the STA, a correlation matrix will standardize the covariance matrix, revealing the strength of linear relationship between pairs of snippets. In Fig. 21, the color plot indicates which values which had a positive relation with the STA. For example, in the range of 78-82, green and dark green colors indicate that those regions have relatively high correlation; these snippets represent a correlation that positively affects the STA.

By analyzing the covariance and correlation matrix, we may reveal underlying structure in the data beyond the simple LFP spike-triggered average. In turn, these tools may be useful for identifying otherwise hidden manifestations of structural or functional remodeling in local neurons surrounding devices in recorded electrophysiological data. Possible interpretations may include:

- *Sources of Spatial Variation.* One interpretation can be that the waveforms representing high variance are spikes from a different neuron but they have less connectivity with the LFP that is being recorded by the electrode, or it is farther away from the LFP than the one that is influencing the LFP more dominantly. Once we separate the values of the diagonal like this, and look at the values that show high correlation in those rows and columns in the correlation matrix, they can be interpreted as snippets which might be generated from the same neuron.
- *Sources of Temporal Variation.* The second interpretation can be that recordings are from the same group of neurons, but across time the neuronal group is modulating its decision, such that the major variation in the LFP is similar to the STA. Because STA is the average of all the LFP snippets a larger number of spikes gave rise to a shape like the STA. In Chapter 1 we discussed how the LFP is affected by different contributors, the fast action potentials ( $\text{Na}^+$ ), the long lasting potentials ( $\text{Ca}^{2+}$ ) and direct electrical communication between gap junctions. So, when the spike occurs we can see a sharp dip in the STA, but we also can see that the STA is affected in range of 2 msec, hinting towards the contribution due to the fast acting potentials. The synchrony might also be affected by the communication through gap junctions, which can increase neuronal synchrony indirectly, affecting the LFP towards the mean behavior captured by the STA.

### 3. Future use of STC as a tool

In the future, we can use STC to investigate the interpretation of structural and functional network remodeling surrounding implanted electrode arrays. Furthermore, we can use it to assess levels of variation in the data which may not be immediately evident using traditional metrics (spike counts, LFP amplitude, etc.). Likewise, we can apply these techniques in the context of gene knockdown to reveal the effects on the STC matrix, across different time points and implant regions.

## Chapter 4

### CONCLUSION

The goal of the thesis was to create signal processing tools to investigate the structural and functional remodeling effects caused by implantation of a neural prosthesis. We begin this by understanding the signal we will be analyzing, as described in the first chapter. In this chapter, we describe how a neuron generates an action potential, how the neuron integrates the various inputs it is receiving, how the signal travels from the soma to the axon terminals, and how these things affect the shape of the action potential generated. Once we understand how a single neuron generates a signal, we consider the activity associated with a broader interconnected population of neurons (the local field potential). We discuss how the shape of the LFP might be affected by different contributors, the geometry of the neuron, the architecture of the arrangement of the neurons, and on the nature of the recording array. We then discuss how the brain reacts to the implant and how different features around the implant are affected, and how this may influence the recorded data. The last part of the chapter discusses the challenges not created by the tissue response, but rather the technical challenges at play.

After understanding the major features influencing the recorded data, we move into the second chapter where we look at data from the LFP and MUA, and how the relationship between them might reflect the connectivity within the network. Here, we discuss the concept of communication through coherence, and how there might exist a frequency where LFP and MUA lock with each other providing maximum communication. The second part of the chapter looks at another signal processing tool known as the spike triggered average (STA), which is conventionally used to study the relationship between spiking and the corresponding stimuli. Here, we use it to look at the synchrony between the spiking and the local field potential. In the last part of the chapter, we

discuss how the results from these tools can be interpreted to reveal the connectivity within the network. In this chapter, we introduce two tools to reveal changes in tissue response by observing the electrical activity: MUA-LFP coherence analysis and LFP-STA.

In the third chapter, we discuss how the tools discussed in the previous chapter reveal only the linear relationship between the signals, which is useful but hides the non-linear features affecting the response. Therefore, in the third chapter we look at a tool which reveals the hidden non-linearities present known as spike triggered covariance and correlation (STC). In the first part of the chapter, we discuss what covariance and correlation mean, building toward calculation of the STC matrix. Next, we discuss how to interpret this matrix and how the features revealed by STC might be responsible in forming the final response we observe in the LFP-STA, and what this might mean in terms of connectivity within the network.

The tools created in the previous chapters are expected to provide us with new insights about what might be happening around the implant when applied on recorded data. Because these tools haven't been used on large data sets to reveal strong conclusions as-of-yet, this thesis serves as an introduction of these tools and a proof-of-principle for their use to understand the functional and structural connectivity. We expect that these tools will be further improved and have more features incorporated in them moving forward.

Nonetheless, while we have only used them on a small dataset, it is already evident that a lot of features may be revealed just through its straightforward/initial application. In the future, we can use these tools on different neuronal populations, or the same tools layered over other analyses. The LFP-STA can be used to look at the tissue response across different time points, and it also can be used along with current source density analysis to get a clearer picture of how the LFP is being constructed. Likewise, it also can be used for spike-triggered average of the time–frequency

spectrum of the LFP (STFFA). All of these analyses, as discussed, can be looked at in parallel with the MUA-LFP coherence. We can also look at how the communication between different neuronal populations is affected within the network. STC analysis can be applied to reveal the non-linearities, which in the case of MUA-LFP coherence might be very informative, and might reveal information about non-linearities in the cortical network in future work.

## APPENDICES

## APPENDIX A: Coherence Analysis

```
1. %% reading the required data files: Raw LFP and Sorts
2. file1 = uigetfile('*.mat'); %LFP raw: gets directory
3. %% Raw data
4. T=load(file1); % Raw Wave
5. b=T.data.Wave.data{1,1};
6. [u1,u2]=size(b);% get the length of arrays in LFP data
7. B=zeros(u2,16); % empty matrix
8. for k=1:16
9. B(:,k)=T.data.Wave.data{1,(k)};% store LFP data in B
10. end
11. %% Select the data file
12. data=B(:,3)% change value of 3 from 1 to 16 depending on which channel you want to see
13. %% Filter MUA
14. S1=filter(MUA,data); % MUA = band pass filter form 300hz-6000hz
15. SD1=std(S1);
16. if abs(S1(:,:))<SD1;
17. S2(:,:)=0;
18. else S2=S1(:,:);
19. end
20. % undo comment if you want to see the effect of clipping
21. % S3=S1-S2;
22. % figure;
```

```

23. % subplot(3,1,1)
24. % plot(S1);
25. % subplot(3,1,2)
26. % plot(S2);
27. % subplot(3,1,3)
28. % plot(S3); % based on these plots theres no values below 2STD
29. RMS1=(S2).^2;
30. S4=filter(rms100,RMS1); % rms100 filter= low pass filter at 100 Hz
31. %% s4
32. s4=downsample(S4,97); % downsample to 500 Hz
33. %% sqrt
34. mua=(s4).^(1/2);% take square root of the mean square s4
35. %% Filter LFP
36. s1=filter(humnoise,data); % Hum noise filter= notch at 60 Hz
37. s2=filter(LFP,s1); % LFP filter= low pass at 300 Hz
38. lfp=downsample(s2,97); % downsample to 500 Hz
39. %% fourier spectrums
40. F1=fft(mua);
41. F2=fft(lfp);
42. [f1,a1]=viewfft(mua,500);
43. [f2,a2]=viewfft(lfp,500);
44. %% LFP plot
45. figure;

```

```
46. plot(a2,f2);
47. title('Fourier Transform LFP');
48. xlabel('Frequency Hz');
49. ylabel('Power V^2');
50. %% Applying the coherence formula
51. o1=F1/length(F1);
52. o2=F2/length(F1);
53. O=abs(o1.*conj(o2)).^2./(abs(o1).^2.*abs(o2).^2);
54. figure;
55. plot(a1,abs(O(1:length(a1)))));
56. xlabel('Frequency Hz');
57. ylabel('Coherence');
```

## APPENDIX B: Local field potential-spike triggered average

1. %% reading the required data files: Raw LFP and Sorts
- 2.
3. file1 = uigetfile('\*.mat'); %LFP raw: gets directory
4. file2 = uigetfile('\*.mat'); %Sorts file: gets directory
- 5.
6. %% plotting mean waveforms: for verification with the next section
7. %uncomment if you want to remove meanwaveforms
8. % A=load(file2); %load sorts in A
9. % Z=A.sorts.meanwaveforms; % Store meanwaveforms in Z: 16x1 structure
10. % [X,Y]=size(Z) % store dimension values in (X,Y)= (16,1)
11. %
12. % for j= 1:X
13. %
14. % z = A.sorts.meanwaveforms{j,:}; % going through variables inside Z indexed by j
15. % [x,y]=size(z); % dimensions of z
16. %
17. % for i=1:x
18. % o = A.sorts.meanwaveforms{j,:}(i,:);
19. % subplot(4,4,j)
20. % plot(o);
21. % title(['Channel ',num2str(j)]);
22. % xlabel('time (msec)');

```

23. % ylabel('volts');
24. % hold on;
25. % end
26. % sgtitle('Meanwaveforms')
27. % legend('MWF 1','MWF 2');
28. % end
29. % hold off;
30. %
31. % %% Eliminating channels without units
32. %
33. % % The loop does the same thing the above loop does but this time it
34. % % compares the first value in the plot with the maximum value in the plot,
35. % % if they are within a tolerance of 6uV it doesn't plot it
36. % % c has the values of channel that need to be plotted
37. %
38. % H=zeros(16,4) % array for storing the starting point and the highest points in the MWF's
39. %           % 4 for each channel
40. % h=zeros(1,4) % array for subtraction of the stored values in the above array
41. % c=zeros(1,16) % storing the values of subtraction
42. % c1=zeros(1,16) % storing values of which meanwaveform was used
43. % % c(1,1:16)=1:16;
44. %
45. % figure;

```

```

46. %
47. % for j= 1:X
48. %
49. % z = A.sorts.meanwaveforms{j,:};
50. % [x,y]=size(z);
51. %
52. % for i=1:x
53. % p = A.sorts.meanwaveforms{j,:}(i,:);
54. % h(i)=abs(abs(p(1))-abs((max(p))));
55. % H(j,i)=h(i);
56. % if ((h(i)>6e-06))
57. %     c(j)=j;
58. %     c1(j)=i;
59. %     subplot(4,4,j)
60. %     plot(p);
61. %     title(['Channel ',num2str(j)]);
62. %     xlabel('Time(msec)')
63. %     ylabel('volts')
64. %     hold on;
65. %     end
66. % end
67. % hold off;
68. % sgtitle('Sorted meanwaveforms')

```

```

69. % end
70. %
71. %% Obtain LFP of the channels with units in a matrix
72.
73. % czero = c(c~=0); % channel numbers with units
74. czero=16;
75. T=load(file1); % raw LFP
76. % cz=length(czero)
77. cz=16;
78. b=T.data.LFPV.data{1,czero(1)};
79. [u1,u2]=size(b);% get the length of arrays in LFP data
80. B=zeros(u2,cz); % empty matrix
81. for k=1:cz
82. B(:,k)=T.data.LFPV.data{1,czero(k)};% store LFP data in B
83. end
84.
85. %% apply fourier on channels with units, plots for time and fourier
86.
87. fourier1=fft(B);
88. [rawpower,axis1]=viewfft(fourier1,3051.8);% view fft is a separate function
89. figure;
90. for k1=1:cz
91. subplot(4,4,k1)

```

```

92. plot(B(:,k1))
93. title(['Channel ',num2str(czero(k1))]);
94. xlabel('Time(msec)')
95. ylabel('volts')
96. end

97. sgtitle('Raw LFP')

98. figure;

99. for k1=1:cz
100.     subplot(4,4,k1)
101.     plot(axis1,rawpower(:,k1))
102.     title(['Channel ',num2str(czero(k1))]);
103.     xlabel('Frequency(Hz)')
104.     ylabel('V')
105. end

106. sgtitle('Fourier Transform')

107. %% Create a time array for the LFP
108.
109. srate=3051.8% sampling rate
110. S=zeros(u2,cz); % empty matrix
111. for k2=1:length(czero)
112.     % S(:,k2)=filter(mid60,B(:,k2));% notch filter
113.     S(:,k2)=B(:,k2);% no notch filter
114. end

```

```

115. len=(length(b))/3051.8;% total number of samples/sampling rate= time in seconds
116. K=1/srate;% distance between each sample= 1/3051.8
117. time=1:K:(len+1);% first array for time
118. Time=time(1:(length(time)-1));% final array for time
119. %% Extract spike information
120.
121. % c1zero = c1(c1~=0); % MWF waveform to be used
122. P = A.sorts.sniptime{czero(1),c1zero(1)};% spike data
123. g=ones(1,length(P));% time axis for spike array
124. q=P(40:end-40); %excluding the first few spike so that the number of samples is >6000
125. u=length(q); % number of spikes
126.
127. %% create window and calculate STA
128.
129. avg=zeros(1,12001);
130. Finalavg=zeros(1,12001);
131. S1=S';
132. S11=S1(1,:);
133.
134. e11=zeros(u,12001);
135.
136. for w=1:u
137.     f=q(w);

```

```

138.     [~,loc]=min(abs(Time-f));
139.     e=(loc-6000):(loc+6000);
140.     e11(w,:)=S11(e);
141.     avg=avg+S11(e);
142. end
143.
144. Finalavg(1,:)=avg/u;
145.
146. %% Time axis for STA: spike occurs at 2.966 msec
147. lensta=(length(Finalavg(1,:)))/3051.8;% total number of samples/sampling rate= time in
    seconds
148. K1=1/srate;% distance between each sample= 1/3051.8
149. timesta=1:K1:(lensta+1);% first array for time
150. Timesta=time(1:(length(timesta)-1));% final array for time
151. Timestanorm=Timesta-2.966;
152. %% plot the STA :spike occurs at 2.966 msec
153.
154. figure;
155. plot(Timestanorm,Finalavg);
156. title('Spike Triggered Average');
157. xlabel('Time(msec)')
158. ylabel('V')
159. %% STA snippets

```

```
160. figure;
161. for d1=1:u
162.     plot(Timestanorm,e11(d1,:));
163.     title('Snippet Overlap');
164.     xlabel('Time(msec)')
165.     ylabel('V')
166.     hold on
167. end
168. hold off;
```

### APPENDIX C: Spike triggered covariance and correlation

```
1. %% reading the required data files: Raw LFP and Sorts
2. %% reading the required data files: Raw LFP and Sorts
3.
4. file1 = uigetfile('*.mat'); %LFP raw: gets directory
5. file2 = uigetfile('*.mat'); %Sorts file: gets directory
6.
7. %% Obtain LFP of the channels with units in a matrix
8.
9. T=load(file1); % Raw Wave
10. b=T.data.LFPV.data{1,1};
11. [u1,u2]=size(b);% get the length of arrays in LFP data
12. B=zeros(u2,16); % empty matrix
13. for k=1:16
14. B(:,k)=T.data.LFPV.data{1,(k)};% store LFP data in B
15. end
16. %% LFP channel to use
17. S5=B(:,3);% can change value of 3 to 1 to 16 depending on the channel you want to look at
18. %% Time array for MUA
19. srate=3051.8% sampling rate
20. len=(length(S5))/3051.8;% total number of samples/sampling rate= time in seconds
21. K=1/srate;% distance between each sample= 1/500
22. time=0:K:(len);% first array for time
```

```

23. Time=time(1:(length(time)-1));% final array for time
24. %% Extract Spike information
25. A=load(file2); %load sorts in A
26. P = A.sorts.snptime{3,1};% spike data
27. g=ones(1,length(P));% time axis for spike array
28. q=P(40:end-40); %excluding the first few spike so that the number of samples is > 6000
29. u=length(q);
30. %% plot spike and LFP together
31. gg=ones(1,length(g));
32. m1=max(S5);
33. figure;
34. stem(q,gg(40:end-40));
35. hold on;
36. plot(Time,100*S5);
37. hold off;
38. %% Sta begins
39. avg=zeros(1,60001);
40. Finalavg3=zeros(1,60001);
41. S=S5';
42. S11=S(1,:);
43. e13=zeros(u,60001);
44.
45. %% time window for sta

```

```

46.
47. for w=1:u
48.     f=q(w);
49.     [~,loc]=min(abs(Time-f));
50.     e=(loc-30000):(loc+30000);
51.     e13(w,:)=S11(e);
52.     avg=avg+S11(e);
53. end
54.
55. Finalavg3=avg/u;
56.
57. %% %% Time axis for STA: spike occurs at 2.966 msec
58. lensta=(length(Finalavg3))/3051.8;% total number of samples/sampling rate= time in seconds
59. K1=1/srate;% distance between each sample= 1/500
60. timesta=0:K1:(lensta);% first array for time
61. Timesta=time(1:(length(timesta)-1));% final array for time
62. Timestanorm3=Timesta-(1.965*5);
63.
64. %% STA plot
65. figure;
66. plot(Timestanorm3,Finalavg3);
67. title('Spike Triggered Average');
68. xlabel('Time(msec)')

```

```

69. ylabel('V')
70.
71. %% Input the spike indexes you want to compare
72. % figure;
73. % subplot(2,1,1)
74. % plot(Timestanorm3',e13(66,:));
75. % hold on;
76. % % plot(e13(66,:));
77. % plot(Timestanorm3',e13(67,:));
78. % plot(Timestanorm3',e13(68,:));
79. % plot(Timestanorm3',e13(69,:));
80. % plot(Timestanorm3',e13(70,:));
81. % plot(Timestanorm3',Finalavg3,'color','k','LineWidth',1.2);
82. % title('a');
83. % xlabel('time(msec)')
84. % ylabel('V')
85. % legend('66','67','68','69','70','STA');
86. % hold off;
87. % subplot(2,1,2)
88. % plot(Timestanorm3',e13(101,:));
89. % hold on;
90. % plot(Timestanorm3',e13(102,:));
91. % plot(Timestanorm3',e13(103,:));

```

```

92. % plot(Timestanorm3',e13(104,:));
93. % plot(Timestanorm3',e13(105,:));
94. % plot(Timestanorm3',Finalavg3,'color','k','LineWidth',1.2);
95. % title('b')
96. % xlabel('time(msec)')
97. % ylabel('V')
98. % legend('78','79','80','81','82','STA');
99. % hold off;
100. %
101. %% snippet Sta
102. figure;
103. for d1=1:u
104.     plot(Timestanorm3,e13(d1,:));
105.     title('Snippet Overlap');
106.     xlabel('Time(msec)')
107.     ylabel('V')
108.     hold on
109. end
110. hold off;
111.
112. %% Covariance Begins
113.
114. % subtracting mean/STA from matrix

```

```

115. rawcov=e13'; % elements cross channels
116. meanrawcov=bsxfun(@minus,rawcov,Finalavg3'); % data-mean: step 1
117.
118. %% step 2: multiplying matrices
119. C=length(Finalavg3)-1;
120. stacovmat=(meanrawcov'*meanrawcov)/C;
121. figure;
122. imagesc(stacovmat);
123. title('Covariance Matrix')
124. xlabel('LFP Snippet number');
125. ylabel('LFP Snippet number');
126. figure;
127. contourf(stacovmat);
128. title('Contour Covariance Matrix')
129. xlabel('LFP Snippet number');
130. ylabel('LFP Snippet number');
131. %% variance
132. % roo=diag(stacovmat);
133. % figure;
134. % plot(q,roo);
135.
136. %% Step 3: correlation matrix
137. newcorrdata=bsxfun(@rdivide,meanrawcov,(std(meanrawcov,[],1)));

```

```
138. corr1=(newcorrdata'*newcorrdata)/C;
139. figure;
140. imagesc(corr1);
141. title('Correlation Matrix')
142. xlabel('LFP Snippet number');
143. ylabel('LFP Snippet number');
144. figure;
145. contourf(corr1);
146. title('Contour Correlation Matrix')
147. xlabel('LFP Snippet number');
148. ylabel('LFP Snippet number');
```

## REFERENCES

## REFERENCES

1. Functional remodeling of subtype-specific markers surrounding implanted neuroprostheses, JW Salatino, BM Winter, MH Drazin, EK Purcell. *Journal of neurophysiology*, 118(1):194-202, 2017.
2. Alterations in ion channel expression surrounding implanted microelectrode arrays in the Brain, JW Salatino, AP Kale, EK Purcell. *bioRxiv*, 518811, 2019.
3. Genetic Modulation at the Neural Microelectrode Interface: Methods and Applications, Winter BM, Daniels SR, Salatino JW, Purcell EK. *Micromachines (Basel)*, 9(10):476, 2018.
4. Measurement of current-voltage relations in the membrane of the giant axon of *Loligo*, A. L. Hodgkin, A. F. Huxley and B. L. Katz. *Journal of Physiology*, 116(4), 424-448, 1952.
5. Currents carried by sodium and potassium ions through the membrane of the giant axon of *Loligo*, A. L. Hodgkin and A. F. Huxley. *Journal of Physiology*. 116(4), 449-472, 1952.
6. The components of membrane conductance in the giant axon of *Loligo*, A. L. Hodgkin and A. F. Huxley, *Journal of Physiology*. 116(4), 473-496, 1952.
7. The dual effect of membrane potential on sodium conductance in the giant axon of *Loligo*, A. L. Hodgkin and A. F. Huxley. *Journal of Physiology*, 116(4): 497–506, 1952.
8. A quantitative description of membrane current and its application to conduction and excitation in nerve, A. L. Hodgkin and A. F. Huxley. *Journal of Physiology*, 117(4), 500-544, 1952.
9. Cellular physiology and neurophysiology, Blaustein, Kao, and Matteson. 2<sup>nd</sup> Edition, 2012.
10. The action potential in mammalian central neurons, Bruce P. Bean. *Nature Reviews Neuroscience*, 8(6):451-465, 2007.
11. The Voltage Sensor in Voltage-Dependent Ion Channels, Francisco Bezanilla. *Physiological Reviews* Vol. 80( 2): 555-592, 2000.
12. The origin of extracellular fields and currents--EEG, ECoG, LFP and spikes. Buzsáki G, Anastassiou CA, Koch C. *Nature Reviews Neuroscience*, 13(6):407-420, 2012.
13. <https://neupsykey.com/neurophysiologic-basis-of-the-electroencephalogram-2/>
14. Nucleus basalis and thalamic control of neocortical activity in the freely moving rat, Buzsáki, G. et al. *Journal of Neuroscience*, 8: 4007–4026, 1988.

15. Sharp wave-associated high-frequency oscillation (200 Hz) in the intact hippocampus: network and intracellular mechanisms, A Ylinen, A Bragin, Z Nadasdy, G Jando, I Szabo, A Sik and G Buzsaki. *Journal of Neuroscience*, 15: 30–46, 1995.
16. Submillisecond synchronization of fast electrical oscillations in neocortex, Barth, D. S. *Journal of Neuroscience*. 23: 2502–2510, 2003.
17. A study of nerve physiology, Lorente de Nó, R. *Studies from the Rockefeller Institute for Medical Research Part I*, 131, 1947.
18. *Electroencephalography: Basic Principles, Clinical Applications, And Related Fields* 5th edn, Niedermayer, Donald L. Schomer & F.H. Lopes da Silva, 2012.
19. The brain in fractal time: 1/f-like power spectrum scaling of the human electroencephalogram, Pritchard W. S. *International Journal of Neuroscience*, 66: 119–129, 1992.
20. Estimation of population firing rates and current source densities from laminar electrode recordings, Pettersen, K. H., Hagen, E. & Einevoll, G. T. *Journal of Computational Neuroscience*, 24:291–313, 2008.
21. Synaptic mechanisms of synchronized gamma oscillations in inhibitory interneuron networks, Bartos, M., Vida, I. & Jonas. P. *Nature Reviews Neuroscience*. 8: 45–56, 2007.
22. Synaptic background activity influences spatiotemporal integration in single pyramidal cells, Bernander, O. Douglas, R. J., Martin, K. A. C. & Koch, C. *Proc. Natl Acad. Sci. USA*, 88: 11569–11573, 1991.
23. Theory of current source-density analysis and determination of conductivity tensor for anuran cerebellum, Nicholson, C. & Freeman, J. A. *Journal of Neurophysiology*, 38: 356–368, 1975.
24. Regenerative Electrode Interfaces for Neural Prostheses, Cort H. Thompson, Marissa J. Zoratti, Nicholas B. Langhals, and Erin K. Purcell. *Tissue Engineering Part B: Reviews*, 22: 125-135, 2016.
25. Fully integrated silicon probes for high-density recording of neural activity, Jun, J., Steinmetz, N., Siegle, J. et al. *Nature* 551: 232–236, 2017.
26. Recent advances in silicon-based neural microelectrodes and microsystems: a review, Zoltan Fekete. *Sensors and Actuators B: Chemical*, 215: 300-315, 2015.
27. Restoring the sense of touch with a prosthetic hand through a brain interface, Tabot GA, Dammann JF, Berg JA, Tenore FV, Boback JL, Vogelstein RJ, Bensmaia SJ. *Proc Natl Acad Sci U S A*, 110:18279-18284.43, 2013.
28. Behavioral assessment of sensitivity to intracortical microstimulation of primate somatosensory cortex, Kim S, Callier T, Tabot GA, Gaunt RA, Tenore FV, Bensmaia SJ. *Proc.*

Natl Acad Sci U S A, 112:15202-15207, 2015.

29. Neural population dynamics in human motor cortex during movements in people with ALS, Pandarinath C, Gilja V, Blabe CH, Nuyujukian P, Sarma AA, Sorice BL, Eskandar EN, Hochberg LR, Henderson JM, Shenoy KV, 4:e07436, 2015.
30. Output properties of the cortical hindlimb motor area in spinal cord-injured rats, Frost SB, Dunham CL, Barbay S, Krizsan-Agbas D, Winter MK, Guggenmos DJ, Nudo RJ. *Journal of Neurotrauma*, 32:1666-1673, 2015.
31. Restoration of function after brain damage using a neural prosthesis, Guggenmos DJ, Azin M, Barbay S, Mahnken JD, Dunham C, Mohseni P, Nudo RJ. *Proc Natl Acad Sci U S A*, 110:21177-21182, 2013.
32. *Neural Prosthetic Systems: Current Problems and Future Directions*, Cindy A. Chestek, John P. Cunningham, Vikash Gilja, Paul Nuyujukian, Stephen I. Ryu, Krishna V. Shenoy, IEEE EMBS, 3369-3375, 2009.
33. Neuronal cell loss accompanies the brain tissue response to chronically implanted silicon microelectrode arrays, Biran, R., Martin, D. C. & Tresco, P. A. *Experimental Neurology*, 195(1): 115-126, 2005.
34. Glial responses to implanted electrodes in the brain JW Salatino, KA Ludwig, TDY Kozai, EK Purcell. *Nature biomedical engineering*, 1(11):862-877 2017.
35. Microthalamotomy effect during deep brain stimulation: Potential involvement of adenosine and glutamate efflux, Y. Shon, Y. M., Agnesi, F. & Lee, K. H. *Annual International Conference of the IEEE Engineering in Medicine and Biology Society* 3294–3297, 2009.
36. Glial responses to implanted electrodes in the brain, JW Salatino, KA Ludwig, TDY Kozai, EK Purcell. *Nature biomedical engineering*, 1: 862–877, 2017.
37. Astrocyte roles in traumatic brain injury, Burda, J. E., Bernstein, A. M. & Sofroniew, M. V. *Experimental Neurology*, 275: 305–315, 2016.
38. Emerging role for astroglial networks in information processing: from synapse to behavior, Pannasch, U. & Rouach, N. *Trends in Neuroscience*, 36: 405–17, 2013.
39. The up-regulation of voltage-gated sodium channel nav1.6 expression following fluid percussion traumatic brain injury in rats Mao, Q. et al. *Neurosurgery*, 66: 1134–1139, 2010.
40. Perspective Multi-scale, multi-modal analysis uncovers complex relationship at the brain tissue-implant neural interface: new emphasis on the biological interface, Nicholas J Michelson<sup>1</sup>, Alberto L Vazquez, James R Eles, Joseph W Salatino, Erin K Purcell, Jordan J Williams, X Tracy Cui and Takashi D Y Kozai. *Journal of Neural Engineering*, 15(3):

033001, 2018.

41. The relationship between glial cell mechanosensitivity and foreign body reactions in the central nervous system, Pouria Moshayedi , Gilbert Ng, Jessica C.F. Kwok, Giles S.H. Yeo, Clare E. Bryant, James W. Fawcett, Kristian Franze, Jochen Guck. *Biomaterials* Volume 35(13): 3919-3925, 2014.
42. Mechanical failure modes of chronically implanted planar silicon-based neural probes for laminar recording, Takashi D.Y. Kozai, Kasey Catt a, Xia Li, Zhannetta V. Gugel, Valur T. Olafsson. *Biomaterials*, 37: 25-39, 2015.
43. Modelling and analysis of local field potentials for studying the function of cortical circuits, Einevoll, Gaute T. et al. *Nature Reviews Neuroscience* 14.11: 770-785, 2013.
44. The gamma cycle, Fries, Pascal, Danko Nikolić, and Wolf Singer. *Trends in neurosciences* 30.\(7): 309-316, 2007
45. Neuronal oscillations in cortical networks, Buzsáki, G., & Draguhn, A. *Science*, 304(5679), 1926-1929, 2004.
46. Modulation of Oscillatory Neuronal Synchronization by Selective Visual Attention, Pascal Fries<sup>1</sup>, John H. Reynolds, Alan E. Rorie<sup>1</sup>, Robert Desimone. *Science*, 291(5508): 1560-1563, 2001.
47. The basis of sensation, Adrian, E. D,W W Norton & Co. 1928.
48. Nonlinear analysis and synthesis of receptive-field responses in the catfish retina. I. Horizontal cell leads to ganglion cell chain, Z Marmarelis , and K I Naka. *Journal of Neurophysiology* 36(4): 605-618, 1973.
49. Triggered Correlation, E. De Boer and P. Kuyper. *IEEE Transactions on Biomedical Engineering*,15(3): 169-179, 1968.
50. Spike initiation by transmembrane current: a white-noise analysis, H L Bryant ,J P Segundo. *The Journal of physiology*, 260(2):279-314, 1976.
51. The Spike-Triggered Average of the Integrate-and-Fire Cell Driven by Gaussian White Noise, Liam Paninski. *Neural Computation*, 18(11): 2592-2616, 2006.
52. Dependence of the spike-triggered average voltage on membrane response properties, Laurent Badel, Wulfram Gerstner, Magnus J.E. Richardson. *Neurocomputing*, 69:1062–1065, 2006.
53. Network Rhythms Influence the Relationship between Spike- Triggered Local Field Potential and Functional Connectivity, Supratim Ray and John H. R. Maunsell. *The Journal of Neuroscience*, 31(35): 12674-12682, 2011.

54. Unsupervised Spike Detection and Sorting with Wavelets and Superparamagnetic Clustering, R. Quian Quiroga, Z. Nadasdy, and Y. Ben-Shaul. *Neural Computation*, 16(8): 1661-1687, 2004.
55. A review of methods for spike sorting: the detection and classification of neural action potentials, Michael S. Lewicki. *Medicine, Computer Science Network*, 9(4):53-78, 1998.
56. Predicting Movement from Multiunit Activity, Eran Stark and Moshe Abeles. *Journal of Neuroscience*, 27 (31): 8387-8394, 2007.
57. Rhythms For Cognition: Communication Through Coherence, Pascal Fries. *Neuron*, Volume 88(1): 220 – 235, 2015.
58. Comparisons of the Dynamics of Local Field Potential and Multiunit Activity Signals in Macaque Visual Cortex. Samuel P. Burns, Dajun Xing, and Robert M. Shapley. *Journal of Neuroscience*, 30(41): 13739-13749, 2010.
59. Neural decoding, Naureen Ghani February 2018.
60. Spike-triggered average electrical stimuli as input filters for bionic vision—a perspective, D L Rathbun, N Ghorbani<sup>1</sup>, H Shabani<sup>1</sup>, E Zrenner, and Z Hosseinzadeh, Liu, J.K., Schreyer, H.M., Onken, A. et al. *Journal of Neural Engineering*, 15(6): 063002, 2018.
61. Spike-triggered neural characterization Odelia Schwartz; Jonathan W. Pillow; Nicole C. Rust; Eero P. Simoncelli. *Journal of Vision*, 6(13): 484-507, 2016.
62. Flavopiridol reduces the impedance of neural prostheses in vivo without affecting recording quality, Erin K Purcell, David E Thompson, Kip A Ludwig, Daryl R Kipke. *Journal of Neuroscience Methods*, 183(2):149-157, 2009.
63. Inference of neuronal functional circuitry with spike-triggered non-negative matrix factorization, Liu, J.K., Schreyer, H.M., Onken, A. et al. *Nature Communications*, 8(149), 2017.
64. Laminar population analysis: estimating firing rates and evoked synaptic activity from multielectrode recordings in rat barrel cortex, Einevoll, G. T. et al. *J. Neurophysiol.* 97: 2174–2190, 2007.
65. Effect of stimulus intensity on the spike–local field potential relationship in the secondary somatosensory cortex, Ray, Supratim, et al. *Journal of Neuroscience* 28(29): 7334-7343, 2008.
66. Characterizing Neural Gain Control using Spike-triggered Covariance, Odelia Schwartz, E.J. Chichilnisky, Eero P. Simoncelli. *Advances in Neural Information Processing Systems*, 14: 269-276, 2001.

67. Spike-Triggered Covariance Analysis Reveals Phenomenological Diversity of Contrast Adaptation in the Retina, Jian K. Liu, Tim Gollisch . PLoS Computational Biology, 11(7): e100442, 2015.
68. Spike-triggered characterization of excitatory and suppressive stimulus dimensions in monkey V1, Nicole C. Rusta, Odelia Schwartz, J. Anthony, Movshona, Eero Simoncellia, Neurocomputing, 58(60): 793-799, 2004.